Manuscript Details

Manuscript number	IJRMMS_2017_299_R1
Title	Dynamic stress concentration and energy evolution of deep-buried tunnels under blasting loads
Article type	Research paper

Abstract

A theoretical formulation was first established to evaluate the dynamic stress concentration factor (DSCF) around a circular opening under conditions of blasting stress wave incidence. A two-dimensional numerical model was then constructed by the particle flow code (PFC) in order to simulate the dynamic responses around an underground tunnel subjected to blasting load. In the simulation, a series of horizontal blasting stress waves were applied to an underground tunnel under various in situ stress states, and then the dynamic responses around the tunnel were analyzed from the viewpoint of the dynamic stress concentration and energy evolution. The results of theoretical analysis indicated that obvious dynamic effects occur at tunnel boundary during blasting stress wave incidence, and the DSCF at the roof and floor of the tunnel is much larger than that at two sidewalls when blasting stress wave was applied to left model boundary. The numerical results showed that high static compressive stress concentration around the underground tunnel results in the accumulation of substantial strain energy at the same location. The roof and floor of the tunnel are more prone to dynamic failures during the blasting loading process. In addition, the analysis of energy dissipation indicated that the strain energy reduction and the residual kinetic energy are positively related to the lateral pressure coefficient and the burial depth of the tunnel, and the residual kinetic energy is much larger than the strain energy reduction under the same condition. Furthermore, for an underground tunnel subjected to high in situ stress, the blasting stress wave with lower amplitude is sufficient to trigger severe dynamic failures.

Keywords	underground tunnel; dynamic stress concentration; energy evolution; blasting load; numerical simulation

Corresponding Author	Chongjin Li
Corresponding Author's Institution	Central South University
Order of Authors	Xibing Li, Chongjin Li, Wenzhuo Cao, Ming Tao

Submission Files Included in this PDF

File Name [File Type]

cover letter.doc [Cover Letter]

Responses to the reviews.doc [Response to Reviewers]

IJRMMS-2017-299-zimmerman.doc [Manuscript File]

Figures and tables.doc [Figure]

Cover letter

Dear editors:

We would like to submit the enclosed manuscript entitled "**Dynamic stress concentration and energy evolution of deep-buried tunnels under blasting loads**" as an article for publication in *International Journal of Rock Mechanics and Mining Sciences*. This paper reports on an investigation into the dynamic stress concentration and energy evolution of underground tunnels subjected to blasting loads with the method of theoretical analysis and numerical simulation. This paper has not been published or partly published in any other journals. All authors agree to submit the paper to your journal.

Thank you very much for your attention and consideration. Please let me know if you have any questions. I'm looking forward to hearing from you soon.

Sincerely yours,

Chongjin Li

E-mail: lcj2015@csu.edu.cn

Responses to the comments

Dear Editor,

Thank you for your letter and for the reviewer's comments concerning our manuscript entitled "**Dynamic stress concentration and energy evolution of deep-buried tunnels under blasting loads" (ID: IJRMMS_2017_299)**. We would like to thank the reviewer for making many thoughtful comments which are valuable and helpful for revising and improving our paper. We have studied the comments carefully and have made corrections which we hope meet with approval.

We mark all the changes in red in the revised manuscript, and the point-to-point responses to the comments are as follows.

Responses to Editor's suggestions

Suggestion 1: Please use 1.5-line spacing, indent the first line of each paragraph, and do not skip a line between paragraphs.

Response: The manuscript has been set as 1.5-line spacing without skipping a line between paragraphs, and each paragraph has been indented accordingly.

Suggestion 2: Please do not use dots to indicate multiplication within an equation.

Response: The dots in the equations have been deleted.

Suggestion 3: Please reduce the number of figures to no more than 12.

Response: The total number of figures has been limited to 12, and detailed modifications are as follows:

(1) The original Fig. 1 has been deleted, and the original section 2.1 has been incorporated into the original section 2.2 (i.e. section 2.1 in the new version).

(2) The original Fig. 3 has been deleted, because this figure is not very necessary in the paper.

(3) The original Figs. 8 and 9 have been substituted by Table 3, and the original section 4.1 has been deleted. The interpretations corresponding to Table 3 have been added to section 4.2 in the new version (lines from 478 to 485).

Suggestion 4: Please do not embed the figures and tables in the text. Each figure and table should be uploaded as a separate file.

Response: The figures and tables in the manuscript have been separated as a separate file entitled 'Figures and tables'.

Responses to reviewer #1

Comment 1: I don't see a close connection between theoretical analysis from theoretical formulation and numerical modeling with PFC. I assume the authors would like to simulate dynamic responses around an underground tunnel with PFC2D based on the theoretical formulation.

Response: Thanks very much for the comment. The main purpose of this paper is to investigate the dynamic stress concentration and energy evolution law around an underground tunnel under blasting load, and the authors believe that the strain energy accumulating around the tunnel is related to the stress concentration. Based on this purpose, we firstly derive a theoretical formulation to study the dynamic stress concentration factor around the tunnel only subjected to blasting load, and the theoretical results validate that the blasting load can induce noticeable dynamic effects at tunnel boundary. However, the underground tunnel has been naturally pre-stressed before subjected to blasting load, the dynamic response of an underground tunnel under coupled static-dynamic stress remains unclear. Therefore, based on the theoretical results, we establish a numerical model using PFC2D to simulate the dynamic response of an underground tunnel under coupled static-dynamic stress, and to further investigate the dynamic failure characteristics of the underground tunnel from the perspective of energy dissipation. The above illustrations of the connection between theoretical analysis and numerical simulation are shown in section 3 (the first paragraph).

In addition, in order to further illuminate the connection between theoretical analysis and numerical simulation, a comparison between theoretical and numerical results was added to section 4.1 (the original section 4.2). The comparison between theoretical analysis and numerical simulation indicates that the numerical results are generally consistent with the theoretical results, i.e. under blasting stress wave incidence, the compressive stress at $\theta = \pi/2$ is much larger than that at $\theta = 0$ and π. However, there are also some differences between theoretical and numerical results, because the theoretical solutions are based on elastodynamics, in which the rock mass is considered as homogeneous, isotropic and perfectly elastic medium, while the numerical model composes of a large number of discrete particles. Besides, the average stress in a measurement circle cannot completely represent the stress on tunnel surface.

Comment 2: Literature review is weak, especially for the review of numerical modeling on dynamic responses around an underground tunnel subjected to blasting load (only three sentences from lines 58 to 63).

Response: Thank you for this comment. To cope with this comment, we tried our best to improve the literature review. Firstly, a review on the dynamic responses of underground structures subjected to blast-induced stress waves was added to the literature review in section 1. Besides, more numerical studies on the dynamic responses of underground structures under blasting load were reviewed, which involved various numerical methods such as the boundary element method (BEM), the finite element method (FEM), the finite difference method (FDM), and so on.

Detailed modifications are shown in section 1.

Comment 3: They missed a lot of recent studies on dynamic responses around an underground tunnel subjected to blasting load, for example:

1) Stamos, A. and D. Beskos, Dynamic analysis of large 3‐D underground structures by the BEM. Earthquake engineering & structural dynamics, 1995. 24(6): p. 917-934.
2) Hao, H., C. Wu, and Y. Zhou, Numerical analysis of blast-induced stress waves in a rock mass with anisotropic continuum damage models part 1: equivalent material property approach. Rock Mechanics and Rock Engineering, 2002. 35(2): p. 79-94.
3) Dhakal, R.P. and T.-C. Pan, Response characteristics of structures subjected to blasting-induced ground motion. International Journal of Impact Engineering, 2003. 28(8): p. 813-828.
4) Wu, C., Y. Lu, and H. Hao, Numerical prediction of blast‐induced stress wave from large‐scale underground explosion. International journal for numerical and analytical methods in geomechanics, 2004. 28(1): p. 93-109.
5) Wang, Z.-L., Y.-C. Li, and R. Shen, Numerical simulation of tensile damage and blast crater in brittle rock due to underground explosion. International Journal of Rock Mechanics and Mining Sciences, 2007. 44(5): p. 730-738.
6) Wang, Z., H. Konietzky, and R. Shen, Coupled finite element and discrete element method for underground blast in faulted rock masses. Soil Dynamics and Earthquake Engineering, 2009. 29(6): p. 939-945.
7) Chen, H., et al., Dynamic responses of underground arch structures subjected to conventional blast loads: Curvature effects. Archives of Civil and Mechanical Engineering, 2013. 13(3): p. 322-333.

Response: Thank you for recommending these excellent works. All of the recommended studies have been included in the references in the revised manuscript. Besides, we also added some other studies on dynamic responses around an underground tunnel subjected to blasting load to improve the literature review.

Detailed modifications are shown in section 1 and references.

Comment 4: Too much self-citation, up to 40 percent of the 13 references by authors out of 35 references in total.

Response: After Reviewer's comment, self-citations which are not quite relevant to the topic were substituted by more classical literature, and only the most relevant literatures by authors were reserved (7 references by the authors out of 51 references in total).

Comment 5: A comparison between numerical results and laboratory tests (complete stress – strain curve and final failure mode) on uniaxial compressive tests of rock from Kaiyang Phosphate Mine as shown in Fig. 6 should be provided.

Response: Thank you for this comment. The complete stress-strain curve and final failure mode of the laboratory test were added to Fig. 4 (the original Fig. 6 has been changed to Fig. 4 in the new version). It can be seen from Fig. 4 that the uniaxial compressive strength and Young's modulus of numerical model are approximately equal to those obtained by experiment test, and the numerical model exhibits the same failure mode as the physical model. However, the peak strain of the experimental stress-strain curve is larger than that of the numerical result, because the real rock specimen usually contains many natural micro-fractures while the numerical model consists of a compacted assembly of rigid particles.

The comparisons between numerical and laboratory results have been add to section 3.1 (lines from 308 to 317).

Comment 6: Line 652. "The conclusions of this study are consistent with their results …". What's their results?

Response: Thank you for this comment. The results of Li and Weng are "the strain energy distribution in tunnel boundary is related to the lateral pressure coefficient, and the strain energy is mainly stored in compressive stress concentration zone under static stress" and "when the lateral pressure coefficient is less than 1.0, two sidewalls of the opening are subjected to high compressive stress, which results in high strain energy intensity near the sidewalls. But when the lateral pressure coefficient is larger than 1.0, the strain energy mainly intensifies at the roof and floor". In our paper, the conclusions from section 4.2 are consistent with their results.

Detailed explanations of the previous results are shown in section 5 (lines from 582 to 587).

Comment 7: A list of symbols should be provided to make it clear.

Response: We agree with Reviewer that a list of symbols can make the paper easier to understand. However, we are uncertain that whether this is essential for the journal, because we have consulted the "Guide for Authors" of this journal and a lot of papers published in this journal, we did not find any information on the list of symbols. So we provide a list of symbols only in this letter (not included in the manuscript). If approved, we will add the list of symbols to the paper.

A list of symbols

A_n and B_n	Expansion coefficients of incident wave function
a	Tunnel radius
BEM	Boundary element method
c_p and c_s	P wave velocity and S wave velocity
D&B	Drill and blast method
DAF	Dynamic amplification factor
DDA	Discontinuous deformation analysis
DEM	Discrete Element Method
DSCF	Dynamic stress concentration factor
E_c and E_{pb}	Strain energy stored in contact and parallel-bond
EDZ	Excavation damaged zone
E_k	Kinetic energy
FDM	Finite difference method
FEM	Finite element method
FEM-DEM	Finite-discrete element method
F_i	Force applied to each boundary particle
$H_n^{(1)}(x)$	First type of Hankel function

$J_n(x)$	First type of Bessel function
k	Lateral pressure coefficient
$P_b(t)$	Blasting load time history
P_{bm}	Peak pressure of the blasting load
$R(\omega)$ and $I(\omega)$	Real and imaginary parts of the frequency response
SED	Strain energy density
t	Time
t_r and t_s	Rising time and total time of the blasting load
UCS	Uniaxial compressive strength
α and β	P wave number and S wave number
$\varepsilon_{ij}^{(k)}$	Contributions of various waves to the stress
κ	Ratio of P to S wave velocity
λ and μ	Lamé constants
σ_{rr}, $\sigma_{\theta\theta}$ and $\sigma_{r\theta}$	Radial stress, tangential stress and shear stress around tunnel
σ_v and σ_h	Vertical and horizontal in situ stress
$\overline{\sigma}_{\theta\theta}$	Dimensionless tangential stress
$\varphi^{(i)}$	Incident wave
$\varphi^{(r)}$ and $\psi^{(r)}$	Reflected P wave and S wave
φ_0	Amplitude of incident wave
ω	Circular frequency
ρ	Rock mass density

Comment 8: Other comments about grammar errors.

1) Lines 15, 242, 685 & 686. Change “large” to “larger”.

2) Line 48. Change “are focused on” to “focus on”.

3) Line 280. Change “dimentional” to “dimensional”.

4) Line 296. Change “Uniaxial” to “uniaxial”.

5) Line 324. Change “modell” to “model”.

6) Line 673. Change “Howere” to “However”.

Response: We are sorry for our negligence. We have checked the manuscript thoroughly and corrected the grammar errors. All grammar corrections in the manuscript are marked in red.

We tried our best to improve the manuscript and made some changes in the manuscript. These changes will not influence the content and framework of the paper. Here we did not list the changes but marked them in red in the revised manuscript. We appreciate the Editor’s and Reviewer’s constructive comments, and hope that the correction will meet with approval. Once again, thank you very much for your comments and suggestions.

IJRMMS_2017_299 – edited and approved by editor

Dynamic stress concentration and energy evolution of deep-buried tunnels under blasting loads

Xibing Li[a, b], Chongjin Li[a, b, *], Wenzhuo Cao[c], Ming Tao[a, b]

[a] School of Resources and Safety Engineering, Central South University, Changsha, Hunan, China

[b] Hunan Key Laboratory of Resources Exploitation and Hazard Control for Deep Metal Mines, Changsha, Hunan, China

[c] Department of Earth Science and Engineering, Imperial College, London SW7 2AZ, United Kingdom

Abstract: A theoretical formulation was first established to evaluate the dynamic stress concentration factor (DSCF) around a circular opening under conditions of blasting stress wave incidence. A two-dimensional numerical model was then constructed by the particle flow code (PFC) in order to simulate the dynamic responses around an underground tunnel subjected to blasting load. In the simulation, a series of horizontal blasting stress waves were applied to an underground tunnel under various in situ stress states, and then the dynamic responses around the tunnel were analyzed from the viewpoint of the dynamic stress concentration and energy evolution. The results of theoretical analysis indicated that obvious dynamic effects occur at tunnel boundary during blasting stress wave incidence, and the DSCF at the roof and floor of the tunnel is much larger than that at two sidewalls when blasting stress wave was applied to left model boundary. The numerical results showed that high static compressive stress concentration around the underground tunnel results in the accumulation of substantial strain energy at the same location. The roof and floor of the tunnel are more prone to dynamic failures during the blasting loading process. In addition, the analysis of energy dissipation indicated that the strain energy reduction and the residual kinetic energy are positively related to the lateral pressure coefficient and the burial depth of the tunnel, and the residual kinetic energy is much larger than the strain energy reduction under the same condition. Furthermore, for an underground tunnel subjected to high in situ stress, the blasting stress wave with lower amplitude is sufficient to trigger severe dynamic failures.

Keywords: underground tunnel; dynamic stress concentration; energy evolution; blasting load; numerical simulation.

---

* Corresponding author.

E-mail address: lcj2015@csu.edu.cn (C. Li)

1. Introduction

In recent years, the exhaustion of mineral resources in shallow depths, and the rapid development of tunneling and hydropower engineering, have considerably motivated the tunnel excavations to extend to depth. However, due to the complicated geological environment in which deep excavations are carried out, a large number of unconventional rock failure phenomena such as spalling,[1, 2] zonal disintegration phenomenon[3, 4] and rockburst hazards[5, 6] have been observed during underground excavations. These accidents or hazards will bring about damages to equipment and delays of excavation operation, and even pose great threats to the safety of construction personnel. Therefore, it is an urgent issue to figure out the mechanism of the engineering disasters occurring in deep excavations.

In practice, underground rocks and ores are naturally stressed by gravitational and tectonic stress. When an underground tunnel is excavated, the previous stress states existing in rock mass are disturbed, with the radial principal stress being released and tangential principal stress concentrating in the periphery of the tunnel.[7-9] In this process, the strain energy releases at some locations while accumulating at other locations, which leads to different mechanical responses of underground tunnels under dynamic disturbance.[10, 11] In addition, during the underground excavation process, the excavation damaged zone (EDZ) is formed in the proximity of the excavated tunnel. To date, considerable research efforts were devoted to investigating the formation of EDZ and the fracture mechanisms of surrounding rock during underground excavations.[12-17] For instance, a series of studies have been carried out at the Underground Research Laboratory (URL) since 1983 to study excavation responses when underground openings were excavated.[13, 14] Findings of these works showed that various factors such as the near-field stress history, geological variability, excavation method, tunnel geometry, and confining pressure are responsible for the excavation damage and instability of underground openings. The presence of the EDZ around an underground opening in turn has a great influence on the mechanical, hydraulic, and thermal characteristics of surrounding rock masses. However, previous research works on the instability of underground openings focus on static and quasi-static conditions, and few reports have considered the effect of dynamic disturbance. Many evidences showed that, during underground excavations, dynamic disturbance such as explosion-induced vibrations from adjacent tunnel and stress impact from neighboring rockbursts have a significant influence on existing tunnels.[18-20] Therefore, the dynamic disturbance is an important factor to be considered when studying the stability of deep-buried tunnel.

The drill and blast (D&B) method is extensively used in mining and tunneling engineering, because it is still an economical and efficient excavation approach for rock fracture and fragmentation.[21] When the drill and blast method is used in underground excavations, the blasting vibration is generated and propagates to the deep of surrounding rock mass in the form of stress waves, which may cause damage to not only the surrounding rock mass but also nearby structures.[22, 23] Therefore, many researchers have conducted a lot of studies on the dynamic responses of structures subjected to blast-induced stress waves, aiming at putting forward more reasonable and effective support schemes. For instance, Malmgren and Nordlund[24] analyzed the dynamic behaviors of shotcrete supported rock wedges subjected to blast-induced vibrations based on field measurement data in the Kiirunavaara mine, and indicated that a wedge can be ejected by a dynamic load even if the static safety factor is larger than 10. Therefore, the support system was suggested to be able to consume energy in order to support the rock wedges subjected to blasting loads. In addition, Dhakal and Pan[25] carried out numerical parametric analyses to investigate the response characteristics of structures subjected to blasting-induced ground motion characterized by short duration, large amplitude and high frequency. Chen et al.[26] theoretically investigated the dynamic responses of underground arch structures subjected to conventional blasting loads, with considering the influence of the curvature of structure surface and the arrival time difference. Their results indicated that the protective structures are better to be constructed in a site with smaller acoustic impedance and larger attenuation factor. Moreover, Mitelman and Elmo[27] pointed out that when the blast-induced stress waves arrive at the tunnel boundary, they are reflected and converted into tensile stress waves, which can cause rock fragments to fly into the tunnel (i.e. spall failure). Based on the modeling results, the authors proposed a new approach for tunnel support designs to withstand spalling induced by blasting loads.

With rapid development of computer technology, numerical simulation techniques have become economical and powerful tools for modeling rock mechanics and rock engineering.[28, 29] Using numerical analysis methods, many researchers have carried out various studies on the dynamic response of rock mass and underground structures under dynamic disturbance. The boundary element method (BEM) was used by Stamos and Beskos[30] to determine the dynamic response of large three-dimensional underground structures subjected to dynamic loads or seismic waves. Wang et al.[31] analyzed dynamic fracture behaviors of rock in tension due to blast loading using a finite element method (FEM) code LS-DYNA. Ning et al.[32, 33] implemented the discontinuous deformation analysis (DDA) to simulate the rock mass failures by the blast-induced high pressure expansion. In their numerical model, the whole process of the blast chamber expansion, explosion gas penetration, rock mass failure and cast, and the formation of the final blasting pile can be wholly reproduced. In addition, the finite difference method (FDM) based program FLAC3D was used by Wang et al.[34] to study the dynamic response of underground gas storage salt cavern under seismic loads. As for dynamic responses of underground tunnels under dynamic disturbance, Zhu et al.[35] used a finite element code RFPA-Dynamics to simulate the rockburst of underground opening triggered by dynamic disturbance; Li and Weng[36] investigated the fracturing behaviors of deep-buried opening subjected to dynamic disturbance using LS-DYNA; Wang and Cai[37] used the SPECFEM2D, a software package based on the spectral element method (SEM), to study the effect of the wavelength-to-excavation span ratio on ground motion near excavation boundaries induced by seismic waves. By making full use of the advantages of various numerical methods, the hybrid finite-discrete element method (FEM-DEM) becomes an alternative numerical method to model blast-induced crack evolution and stress wave propagation in rock mass.[38, 39] Recently, the discrete element method (DEM) code PFC2D was used to study the dynamic features of stress wave propagating through rock joints[40, 41] and to simulate the excavation unloading process of underground tunnel in high stress rock mass. [42, 43] These works validated the feasibility and accuracy of PFC2D to simulate the dynamic process of rock. However, few numerical models were established by PFC2D to simulate the dynamic failure characteristics of underground tunnels subjected to blasting load.

This paper reports on an investigation into the dynamic stress concentration and energy evolution of an underground tunnel during blasting loading process. A two-dimensional mathematical physical model with a circular hole was first established to determine the dynamic stress concentration factor (DSCF) around tunnel boundary under blasting stress wave incidence. Using the theoretical formulations, DSCF and dynamic effects at tunnel boundary was obtained. Then a two-dimensional numerical simulation model established by PFC2D was introduced to verify against the theoretical solution. Based on the numerical model, the distributions of tangential stress and strain energy around a circular tunnel under different in situ stress states were first discussed, and then parametric analyses were carried out to investigate the evolution and dissipation of strain energy around an underground tunnel under different in situ stress environments and various waveforms of blasting stress wave. Findings of the present study indicated that dynamic disturbance and high in situ stress are two important factors to trigger dynamic failure around an underground tunnel. This paper provides an insight into the mechanism of rockbursts in the periphery of underground tunnels, as well as guidance for the design and support of deep-buried tunnels.

2. Theoretical formulation of the dynamic response of a circular hole

2.1. Dynamic response behaviors of circular hole under harmonic wave incidence

In theoretical analysis, it is assumed that a circular tunnel is excavated along the direction parallel to the principal stress, so the problem can be approximately regarded as a plane strain case. For an underground tunnel subjected to dynamic stress waves, according to the superposition principle,[44] the stress, displacement and velocity components of the rock mass around the tunnel can be obtained by superimposing the static component induced by in situ stress with the dynamic component induced by incident plane wave under unstressed condition. However, due to the stress and deformation induced by in situ stress are time-independent, the dynamic stress wave is only considered when theoretically investigating the dynamic response of underground tunnel. In the view of wave mechanics, the problem of the interactions between stress wave and underground opening can be regard as the initial-boundary value problem of wave equation. In this section, we focus on the dynamic responses of underground tunnel subjected to blasting load, which can be simplified as an analysis of circular hole subjected to a plane P wave as shown in Fig. 1, where x and y are the Cartesian coordinate system, θ and r are the Polar coordinate system, and a is the radius of tunnel. As the transient response induced by any form of transient loading can be determined by superposing harmonic waves of all frequencies, it is necessary to first determine a theoretical formulation under harmonic wave excitation, which was described in detail by Mow and Pao.[45]

As shown in Fig. 1, a harmonically time-varying incident plane P wave propagates along the positive direction of axis x, and the incident wave can be expressed as:

$$\varphi^{(i)} = \varphi_0 e^{i(\alpha x - \omega t)} \tag{1}$$

where $\alpha = \omega/c_p$ is the P wave number, φ_0 is the amplitude, ω is the circular frequency, and c_p is the P wave velocity.

In terms of the wave function expansion method, the incident wave function can be expanded as:

$$\varphi^{(i)} = \varphi_0 \sum_{n=0}^{\infty} \varepsilon_n i^n J_n(\alpha r)\cos(n\theta) e^{-i\omega t} \tag{2}$$

where $J_n(x)$ is the first type of Bessel function, and $\varepsilon_n = \begin{cases} 1 & \text{n=0} \\ 2 & \text{n} \geq 1 \end{cases}$.

When an incident plane P-wave propagates through a circular hole, a compressional wave (P wave) and a shear wave (SV wave) arise from the circular hole boundary, because the reflecting surface is not perpendicular to the direction of P wave incidence. The SH wave is not generated because it causes rock particles to oscillate perpendicular to the analyzed plane.[44] P and SV waves can be expressed as:

$$\varphi^{(r)} = \sum_{n=0}^{\infty} A_n H_n^{(1)}(\alpha r)\cos(n\theta)e^{-i\omega t} \tag{3}$$

$$\psi^{(r)} = \sum_{n=0}^{\infty} B_n H_n^{(1)}(\beta r)\sin(n\theta)e^{-i\omega t} \tag{4}$$

where $\varphi^{(r)}$ and $\psi^{(r)}$ are the reflected P wave and the reflected S wave, respectively, which represent waves diverging from the origin, $\beta = \omega/c_s$ is the S wave number, c_s is the S wave velocity, $H_n^{(1)}(x)$ is the first type of Hankel function, A_n and B_n are coefficients of the expressions that can be determined from the appropriate boundary conditions.

The total wave in rock mass can be obtained by adding the reflected wave to the incident wave:

$$\varphi = \varphi^{(i)} + \varphi^{(r)} = \sum_{n=0}^{\infty} [\varphi_0 \varepsilon_n i^n J_n(\alpha r) + A_n H_n^{(1)}(\alpha r)\cos(n\theta)]e^{-i\omega t} \tag{5}$$

$$\psi = \psi^{(r)} = \sum_{n=0}^{\infty} B_n H_n^{(1)}(\beta r)\sin(n\theta)e^{-i\omega t} \tag{6}$$

Radial stress σ_{rr}, tangential stress $\sigma_{\theta\theta}$ and shear stress $\sigma_{r\theta}$ can be described in terms of displacement potential:

$$\sigma_{rr} = \lambda \nabla^2 \varphi + 2\mu \left[\frac{\partial^2 \varphi}{\partial r^2} + \frac{\partial}{\partial r}\left(\frac{1}{r}\frac{\partial \psi}{\partial \theta} \right) \right] \tag{7}$$

$$\sigma_{\theta\theta} = \lambda \nabla^2 \varphi + 2\mu \left[\frac{1}{r}\frac{\partial \varphi}{\partial r} + \frac{1}{r^2}\frac{\partial^2 \psi}{\partial \theta^2} + \left(\frac{1}{r^2}\frac{\partial \psi}{\partial \theta} - \frac{1}{r^2}\frac{\partial^2 \psi}{\partial r \partial \theta} \right) \right] \tag{8}$$

$$\sigma_{r\theta} = \mu \left\{ 2\left[\frac{1}{r}\frac{\partial^2 \varphi}{\partial r \partial \theta} - \frac{1}{r^2}\frac{\partial \varphi}{\partial \theta} \right] + \left[\frac{1}{r^2}\frac{\partial^2 \psi}{\partial \theta^2} - r\frac{\partial}{\partial r}\left(\frac{1}{r}\frac{\partial \psi}{\partial r} \right) \right] \right\} \tag{9}$$

where λ and μ are Lamé constants.

By substituting Eqs. (5) and (6) into Eqs. (7), (8) and (9), we obtain:

$$\sigma_{rr} = \frac{2\mu}{r^2}\sum_{n=0}^{\infty}\left(\varepsilon_n i^n \varphi_0 \varepsilon_{11}^{(1)} + A_n \varepsilon_{11}^{(3)} + B_n \varepsilon_{12}^{(3)} \right)\cos\left(n\theta\right)e^{-i\omega t} \tag{10}$$

$$\sigma_{r\theta} = \frac{2\mu}{r^2}\sum_{n=0}^{\infty}\left(\varepsilon_n i^n \varphi_0 \varepsilon_{41}^{(1)} + A_n \varepsilon_{41}^{(3)} + B_n \varepsilon_{42}^{(3)} \right)\sin\left(n\theta\right)e^{-i\omega t} \tag{11}$$

$$\sigma_{\theta\theta} = \frac{2\mu}{r^2}\sum_{n=0}^{\infty}\left(\varepsilon_n i^n \varphi_0 \varepsilon_{21}^{(1)} + A_n \varepsilon_{21}^{(3)} + B_n \varepsilon_{22}^{(3)}\right)\cos\left(n\theta\right)e^{-i\omega t} \tag{12}$$

where $\varepsilon_{11}^{(1)}, \varepsilon_{11}^{(3)}, \varepsilon_{21}^{(1)} \cdots$ etc. are defined as a part of the contributions to the stresses due to various waves, and the superscripts represent the type of Bessel function.[45]

The boundary condition at $r = a$ is $\sigma_{rr}\big|_{r=a} = 0,\ \sigma_{r\theta}\big|_{r=a} = 0$, thus A_n and B_n can be obtained from the boundary condition:

$$A_n = -\varepsilon_n i^n \varphi_0 \frac{\begin{vmatrix} E_{11}^{(1)} & E_{12}^{(3)} \\ E_{41}^{(1)} & E_{42}^{(3)} \end{vmatrix}}{\begin{vmatrix} E_{11}^{(3)} & E_{12}^{(3)} \\ E_{41}^{(3)} & E_{42}^{(3)} \end{vmatrix}} \tag{13}$$

$$B_n = -\varepsilon_n i^n \varphi_0 \frac{\begin{vmatrix} E_{11}^{(3)} & E_{11}^{(1)} \\ E_{41}^{(3)} & E_{41}^{(1)} \end{vmatrix}}{\begin{vmatrix} E_{11}^{(3)} & E_{12}^{(3)} \\ E_{41}^{(3)} & E_{42}^{(3)} \end{vmatrix}} \tag{14}$$

where $E_{11}^{(3)} \cdots$ is the value of $\varepsilon_{11}^{(3)} \cdots$ evaluated at $r = a$.

The stress field around the tunnel can be determined once the coefficients A_n and B_n are known. In this paper, we are interested in the dynamic responses at tunnel boundary, in which the tangential stress only exists. By substituting Eqs. (13) and (14) into Eq. (12), and letting $r = a$, we obtain the tangential stress at tunnel boundary:

$$\sigma_{\theta\theta}\big|_{r=a} = \frac{4}{\pi}\mu\beta^2\varphi_0\left(1 - \frac{1}{\kappa^2}\right)\sum_{n=0}^{\infty}\varepsilon_n i^{n+1} s_n \cos(n\theta)e^{-i\omega t} \tag{15}$$

where κ is the ratio of P to S wave velocity, $\kappa = \frac{c_p}{c_s} = \frac{\beta}{\alpha} = \sqrt{\frac{\lambda + 2\mu}{\mu}}$, and

$$S_n = \frac{N_n}{D_n} \tag{16}$$

$$N_n = (n^2 - 1)\beta a H_{n-1}^{(1)}(\beta a) - (n^3 - n + \frac{1}{2}\beta^2 a^2) H_n^{(1)}(\beta a) \tag{17}$$

$$D_n = \alpha a H_{n-1}^{(1)}(\alpha a) N_n - H_n^{(1)}(\alpha a)\left[(n^3 - n + \frac{1}{2}\beta^2 a^2)\beta a H_{n-1}^{(1)}(\beta a) - (n^2 + n - \frac{1}{4}\beta^2 a^2) H_n^{(1)}(\beta a)\right] \tag{18}$$

When an incident P-wave propagates in the intact rock medium, the stress intensity of the P wave in the propagation direction is given by $\sigma_0 = \mu\beta^2\varphi_0$. This can serve as the normalized factor, and then the dynamic stress concentration factor (DSCF) at tunnel boundary can be defined as the ratio of $\sigma_{\theta\theta}$ to σ_0:

$$\bar{\sigma}_{\theta\theta}\big|_{r=a} = \frac{\sigma_{\theta\theta}}{\sigma_0} = \frac{4}{\pi}\left(1-\frac{1}{\kappa^2}\right)\sum_{n=0}^{\infty}\varepsilon_n i^{n+1} s_n \cos(n\theta)e^{-i\omega t} \tag{19}$$

2.2. Dynamic responses of a circular hole under transient wave incidence

The steady-state responses of a circular tunnel under a harmonic P-wave have been obtained in section 2.1. In practice, we are more interested in the transient responses of the tunnel under an aperiodic disturbance such as blasting load. In order to obtain the transient responses of the tunnel induced by blasting load, it is necessary to first determine the blast load variation applied to the model boundary.

In blasting process, the explosion-induced load variation is extremely complex in time domain, especially if several deferred-time detonation segments are adopted in the excavations. Therefore, it is necessary to seek a relatively simple equivalent blast loading curve in theoretical and numerical analysis. Based on previous publications relating to blasting procedures,[11, 36, 46] the blasting load can be simplified as a triangular load. The entire blasting processes can be reduced to linear loading and linear unloading process, which can be expressed as:

$$P_b(t) = \begin{cases} 0 & , \ t < 0 \\ \dfrac{t}{t_r} P_{bm} & , \ 0 \le t < t_r \\ \dfrac{t_s - t}{t_s - t_r} P_{bm} & , \ t_r \le t < t_s \\ 0 & , \ t \ge t_s \end{cases} \tag{20}$$

where $P_b(t)$ represents the blasting load time history, P_{bm} is the peak pressure of the blasting load, t_r and t_s are the rising time and total time of the blasting load, respectively. Therefore, the blasting load is regarded as a triangular loading curve to study the transient response of the underground tunnel in the following sections of this paper.

In the model, time begins when the incident wave arrives at the tunnel boundary (i.e., time is zero at $x = -a$). The elapsed time t is normalized by the time required to travel through the length of a radius:

$$\tau = \frac{c_p t}{a} \tag{21}$$

The Fourier transform technique bridges the gap between the steady-state and transient response. For any input function $f(t)$, the transient response of the system can be given by:

$$g(x_i, t) = \frac{1}{\sqrt{2\pi}}\int_{-\infty}^{\infty} \chi(x_i, \omega)F(\omega)e^{-i\omega t}d\omega \tag{22}$$

where $\chi(x_i, \omega)$ is the admittance function, which is defined as the steady-state response of the system when the force source has a magnitude of unit, and $F(\omega)$ is the Fourier transformed form of input function $f(t)$.

In this paper, we are mainly concerned about the transient stress behaviors at the tunnel boundary, and then the frequency response part of Eq. (19) is precisely the admittance function that we need for the problem. Thus, we first take the Fourier transform of $f(t)$ and substitute it together with Eq. (19) into Eq. (22), and then we can obtain the formal expression for the transient behavior of $\sigma_{\theta\theta}$ at tunnel boundary. However, as long as we know the transient response due to a Heaviside step function, we can easily determine the transient response induced by any input function using the Duhamel integral.[45]

The Fourier transform of the Heaviside step function input along the tunnel boundary is given by:

$$F(\zeta) = \frac{i}{\sqrt{2\pi}\zeta}, \qquad \mathrm{Im}\zeta > 0 \tag{23}$$

where $\mathrm{Re}\zeta = \alpha a$. By substituting Eqs. (19) and (23) into Eq. (22), we obtain the DSCF at $r = a$ induced by a Heaviside step input:

$$\bar{\sigma}_{\theta\theta}(t)\Big|_{r=a} = \frac{2i}{\pi^2}\left(1 - \frac{1}{\kappa^2}\right)\sum_{n=0}^{\infty} \varepsilon_n i^{n+1} \cos(n\theta) \int_{-\infty+i\gamma}^{\infty+i\gamma} \frac{S_n e^{-i\zeta t}}{\zeta} d\zeta \tag{24}$$

Theoretically, we can obtain the transient stress behaviors at the tunnel boundary induced by any form of input function from Eq. (22), and this theoretical solution can be solved by using a contour integral, which is an extremely complex integral method. For instance, it is intractable and time-consuming to obtain numerical solutions from Eq. (24) due to the complex integral paths and mathematical difficulties. Accordingly, an approximate method referred to as Trapezoidal Approximation[47] was employed to obtain the numerical transient wave excitation results.

The admittance function of system can be simplified as:

$$\chi(x_i, \omega) = R(\omega) + iI(\omega) \tag{25}$$

where $R(\omega)$ and $I(\omega)$ are the real and imaginary parts of the frequency response.

For a causal function, the transient response can be expressed alternatively in terms of sine or cosine transforms. When the input is an impulse function, the impulse response can be expressed by:

$$g_\delta(x_i, t) = \frac{2}{\pi}\int_0^\infty R(\omega)\cos\omega t \, d\omega \tag{26}$$

Then the response due to a Heaviside step input can be obtained from the integral of the impulse response:

$$g_h(x_i, t) = \int_0^t g_\delta(x_i, \tau) d\tau \tag{27}$$

By substituting Eq. (26) into (27), we obtain:

$$g_h(x_i,t)=\frac{2}{\pi}\int_0^t \cos\omega\tau d\tau\int_0^\infty R(\omega)d\omega=\frac{2}{\pi}\int_0^\infty \frac{R(\omega)\sin\omega t}{\omega}d\omega \tag{28}$$

According to the Duhamel integral, responses to an arbitrary input function $f(\tau)$ can be derived from:

$$g(x_i,t)=\int_0^t f(\tau)g_h^{'}(t-\tau)d\tau \tag{29}$$

After integrating by parts, we obtain:

$$g(x_i,t)=f(0)g_h(t)+\int_0^t f^{'}(\tau)g_h(t-\tau)d\tau \tag{30}$$

In this paper, we focus on the transient responses induced by blasting load, so the input function can be described as:

$$f(t)=\begin{cases}0 & ,\ t<0\\ \dfrac{t}{t_r} & ,\ 0\le t<t_r\\ \dfrac{t_s-t}{t_s-t_r} & ,\ t_r\le t<t_s\\ 0 & ,\ t\ge t_s\end{cases} \tag{31}$$

When $0\le t<t_r$, we have:

$$g(x_i,t)=\int_0^t \frac{1}{t_r}d\tau\frac{2}{\pi}\int_0^\infty \frac{R(\omega)\sin\omega(t-\tau)}{\omega}d\omega=\frac{2}{\pi t_r}\int_0^\infty \frac{R(\omega)(1-\cos\omega t)}{\omega^2}d\omega \tag{32a}$$

When $t_r\le t<t_s$, we have:

$$\begin{aligned}g(x_i,t)&=\int_0^{t_r}\frac{1}{t_r}d\tau\frac{2}{\pi}\int_0^\infty \frac{R(\omega)\sin\omega(t-\tau)}{\omega}d\omega+\int_{t_r}^{t}\frac{-1}{t_s-t_r}d\tau\frac{2}{\pi}\int_0^\infty \frac{R(\omega)\sin\omega(t-\tau)}{\omega}d\omega\\&=\frac{2}{\pi t_r}\int_0^\infty \frac{R(\omega)[\cos\omega(t-t_r)-\cos\omega t]}{\omega^2}d\omega-\frac{2}{\pi(t_s-t_r)}\int_0^\infty \frac{R(\omega)[1-\cos\omega(t-t_r)]}{\omega^2}d\omega\end{aligned} \tag{32b}$$

When $t\ge t_s$, we have:

$$\begin{aligned}g(x_i,t)&=\int_0^{t_r}\frac{1}{t_r}d\tau\frac{2}{\pi}\int_0^\infty \frac{R(\omega)\sin\omega(t-\tau)}{\omega}d\omega+\int_{t_r}^{t_s}\frac{-1}{t_s-t_r}d\tau\frac{2}{\pi}\int_0^\infty \frac{R(\omega)\sin\omega(t-\tau)}{\omega}d\omega\\&=\frac{2}{\pi t_r}\int_0^\infty \frac{R(\omega)[\cos\omega(t-t_r)-\cos\omega t]}{\omega^2}d\omega-\frac{2}{\pi(t_s-t_r)}\int_0^\infty \frac{R(\omega)[\cos\omega(t-t_s)-\cos\omega(t-t_r)]}{\omega^2}d\omega\end{aligned} \tag{32c}$$

Now we can determine the transient stress behaviors of the tunnel under blasting load using Eq. (32). However, it is also cumbersome to take a direct integration of Eq. (32) due to the difficulties associated with obtaining analytical expression of $R(\omega)$. In this paper, $R(\omega)$ is precisely the real part of Eq. (19), which can be obtained by determining the relationship between $\overline{\sigma_{\theta\theta}}$ and all wave numbers using Eq. (19). Once we have the numerical results of $R(\omega)$ with all wave numbers, we can substitute them with a sum of trapezoid functions. In turn, the sum of the simple responses can yield the total dynamic responses.[47] This approach has proved to be an effective way to determine dynamic responses of tunnel subjected to transient loads.[44, 48] The numerical integration mentioned above can be calculated by a MATLAB code.

2.3. Numerical results and analysis

In this section, the physical properties of the rock specimen extracted from the Kaiyang Phosphate Mine were employed to calculate the dynamic responses mentioned above. The density, Yong's modulus and Poisson's ratio of the rock specimen are 2750 kg/m^3, 18.73 GPa and 0.206, respectively. The numerical results of the DSCF variations at the tunnel boundary are presented in Fig. 2, where τ_r is the normalized rising time of the blasting load, and t_s/t_r is the ratio of the total time to the rising time, which characterizes the unloading speed during blasting load. The smaller the t_s/t_r ratio is, the faster the unloading speed it means. When $t_s/t_r = 1$, it means instantaneous unloading of blasting load. As the dynamic responses are related to the observation locations and loading parameters, DSCF variations at $\theta = 0$, $\pi/2$ and π with $t_s/t_r = 5$ and 10 are shown in Fig. 2.

Numerical results in Fig. 2 indicate that obvious dynamic stress concentration generated at tunnel boundary during blasting loading process, which is characterized by compressive stress concentration at $\theta = \pi/2$ and tensile stress concentration at $\theta = 0$ and π. The DSCF at $\theta = \pi/2$ is much larger than that at $\theta = 0$ and π. The DSCF time-history curves at $\theta = 0$ and π have approximately the same shapes. In loading process, DSCF increases rapidly to the first positive peak value and then declines to the minimum value; in unloading process, DSCF increases from the minimum value to the secondary positive peak value and then decreases to zero. While the DSCF curves at $\theta = \pi/2$ have different shapes, only one positive peak value and one negative peak value appear during loading and unloading process. In the entire processes, the loading effect can be represented by the minimum value at $\theta = 0$ and π and maximum value at $\theta = \pi/2$, and the unloading effect can be represented by the secondary positive peak value at $\theta = 0$ and π and negative peak value at $\theta = \pi/2$. It is found that the unloading effect is more dramatic when $t_s/t_r = 5$ than that when $t_s/t_r = 10$. For the same t_s/t_r ratio, the shorter the τ_r is, the more dramatic unloading effect is. It indicates that shorter duration of blasting load induces more obvious unloading effect. When the duration of blasting load increases to $\tau_s = 200$, the unloading effect becomes virtually unnoticeable. With the increase of τ_r, the loading effect converges to the static stress concentration factor, which is given by:[45]

$$\sigma^*_{\theta\theta} = \frac{2}{\kappa^2}\left[\left(\kappa^2 - 1\right) - 2\cos 2\theta\right] \tag{33}$$

where κ is the ratio of P to S wave velocity.

Equation (33) is the limit of Eq. (19) when $\alpha \to 0$, which is equivalent to the static solution for biaxial loadings. The static stress concentration factor is 2.74 at $\theta = \pi/2$ and -0.22 at $\theta = 0$ and π. The dynamic amplification factor (DAF) is introduced to analyze the dynamic effect induced by blasting load, which is defined as:

$$\mathrm{DAF} = \frac{(\overline{\sigma}_{\theta\theta})_{\mathrm{m}} - \sigma^*_{\theta\theta}}{\sigma^*_{\theta\theta}} \times 100\% \tag{34}$$

where $(\overline{\sigma}_{\theta\theta})_{\mathrm{m}}$ is the minimum value of DSCF at $\theta = 0$ and π and the maximum value at $\theta = \pi/2$, and $\sigma^*_{\theta\theta}$ is the static stress concentration factor.

The correlations between dynamic amplification factor and loading parameters at $\theta = 0$, $\pi/2$ and π are shown in Fig. 3, where only the positive values represent the dynamic effect. It is found that DAF increases first and then decreases with the increase of τ_r, and tends to zero when τ_r approaches infinity, which denotes that the dynamic response converges towards static response when τ_r approaches infinity. The maximum DAF at $\theta = \pi/2$ and π are 5.19% and 65.98% when $t_s/t_r = 20$, while the maximum DAF at $\theta = 0$ is 107.36% when $t_s/t_r = 2$. It is worthwhile noting that the DAF is much larger at $\theta = 0$ and π than that at $\theta = \pi/2$, which is contrary to the DSCF.

3. Numerical model descriptions

The DSCF at tunnel boundary induced by blasting load was investigated in terms of theoretical formulation in the above section, and the theoretical results indicated that the blasting load can induce noticeable dynamic effects at tunnel boundary. However, only the dynamic part was taken into consideration when defining the DSCF in the above theoretical computation without considering in situ stress. Actually, the underground tunnel has been naturally pre-stressed before subjected to dynamic disturbance, and the deeper the tunnel locates, the higher the stress level becomes. If coupled static-dynamic stress is considered in this analysis, the quantitative influence of dynamic effect remains unclear. In order to get a further insight into the dynamic effects of underground tunnel under coupled static-dynamic stress, a two-dimensional numerical model established by the discrete element code PFC2D was employed to simulate the dynamic responses of an underground tunnel, and to further investigate dynamic failure characteristics of underground tunnels from the perspective of energy dissipation.

3.1. Calibration of particle parameters and PFC model setup

In PFC2D model, the rock material is represented by an assembly of rigid circular disks bonded together at their contact points. Two basic bond models are provided in PFC2D: the contact-bond model and the parallel-bond model. The parallel-bond has a finite size that acts over either circular or rectangular cross section between the particles, whereas the contact-bond acts only at the contact point due to its vanishingly small size. Therefore, the contact-bond can only resist the force acting at the contact, while the parallel-bond can resist both the force and moment. The parallel-bond model is proved to be a more realistic bond model for rock-like materials,[49] which was used in our PFC model.

The parallel-bond model is characterized by two sets of primary microscopic parameters. One set consists of the microscopic deformation parameters, namely the contact normal and shear stiffness, k_n and k_s, and the parallel-bond normal and shear stiffness, $\bar{k}_n$ and $\bar{k}_s$, which account for the macroscopic deformation behavior. The other set of microscopic strength parameters consists of the contact normal and shear strength, σ and τ, and the parallel-bond normal and shear strength, $\bar{\sigma}$ and $\bar{\tau}$, which dominate the macroscopic strength characteristics and failure modes along with the microscopic deformation parameters. These microscopic parameters should be adjusted to reproduce the macroscopic properties of the real specimen under uniaxial compression such as Young's modulus, uniaxial compressive strength (UCS) and Poisson's ratio, and this adjustment is done by a calibration process associated with a series of trial and error tests. The rock mass in the Kaiyang Phosphate Mine in China was tested, and the corresponding numerical uniaxial compression test model was established for the calibration. The comparisons between experimental and numerical results of the rock specimen under uniaxial compression are shown in Fig. 4 and Table 1, and the calibrated microscopic parameters of the parallel-bond model are presented in Table 2. It can be seen from Fig. 4 and Table 1 that the uniaxial compressive strength and Young's modulus of numerical model are approximately equal to those obtained by experiment test, and the numerical model exhibits the same failure mode as the physical model. These comparisons indicate the reasonability of the calibrated microscopic parameters in Table 2. It is worth noting that the peak strain of the experimental stress-strain curve is larger than that of the numerical result, because the real rock specimen usually contains many natural micro-fractures while the numerical model consists of a compacted assembly of rigid particles.

A 10 m × 10 m rectangular numerical model containing 32,538 particles was established in PFC2D, as shown in Fig. 5a. The radii of the particles ranged from 0.02 to 0.04 m and followed a uniform distribution. The particles were regarded as a series of circular disks with unit thickness, and the linear contact model was adopted at the contact of two particles. Particles with less than three contacts were eliminated via the floater-elimination procedure, and then the parallel-bond model was set at the contact of two particles. An undamped system was adopted for the sake of comparison against the theoretical solution and energy calculation. The in situ stress field of the Kaiyang Phosphate Mine was employed in this simulation, and the fitting equations of the vertical principal stress, maximum horizontal principal stress and minimum horizontal principal stress are presented, respectively, as follows:[44]

$$\sigma_v = 0.74 + 0.014h \tag{35}$$

$$\sigma_{H\max} = 2.76 + 0.028h \tag{36}$$

$$\sigma_{H\min} = 1.83 + 0.017h \tag{37}$$

The numerical modeling processes in the current study involve two parts: in situ stress initialization and dynamic loading. In this paper, we are only concerned about the dynamic responses induced by blasting load without considering the excavation effect, so a circular tunnel with radius 1.0 m was excavated before static stress initialization, and then the in situ stress was applied to the model boundary with a low loading rate. Finally, a series of blasting stress waves were applied to the left boundary of the model to investigate the dynamic responses of an underground tunnel.

In order to investigate the stress and energy evolution of the deep-buried tunnel during blasting loading process, three stress measurement circles (A1, B1, C1) and three energy measurement circles (A2, B2, C2) were set at left sidewall, roof and right sidewall of the tunnel as shown in Fig. 5b. The radii of stress measurement circles and energy measurement circles are 0.2 m and 0.5 m, respectively. It is unworkable to measure stress at PFC2D model boundary, so the center of the stress measurement circle was set at r = 1.2 m. The center of energy measurement circle was set at r = 1.0 m to monitor the evolution of strain energy and kinetic energy during blasting stress waves propagating through the tunnel.

3.2. Model boundary conditions

In numerical simulation, the model boundary condition is a very important factor for simulation results, especially in dynamic numerical simulation. PFC2D provides both the wall and particle boundaries, and the latter was adopted in the present study so that various boundary conditions can be applied.[40] A strip of particles is identified as boundary particles at model boundary as shown in Fig. 5c. The width of the strip is defined with enough size to leave no part of the model unbounded.

In the DEM-based code PFC2D, external loads applied to the model boundary must be translated into forces that are applied to the particles centers since stress is a concept valid only in continuous material. If a stress value σ_0 is to be applied at a cylindrical particle with unitary thickness, the equivalent force applied to the particle must take into account the transversal area of the particle:

$$F_{ball} = \sigma_0 A_{ball} = 2\sigma_0 r_{ball} \tag{38}$$

where r_{ball} is the radius of the particle.

If a static stress value σ_s is applied to the model boundary, the resultant force applied to the boundary particles is:

$$F_{boundary} = \sigma_s A_{boundary} = \sigma_s L \tag{39}$$

where L is the length of the particle boundary.

In order to convert boundary force into particle force, the border width must be taken into consideration. Supposing the force applied to each boundary particle is proportional to the transversal area of the particle, thus the force applied to every boundary particle can be expressed as:

$$F_i = F_{boundary} \frac{2r_i}{\sum_{j=1}^{N_b} 2r_j} = \frac{\sigma_s L r_i}{\sum_{j=1}^{N_b} r_j} \tag{40}$$

where F_i and r_i are the applied force and radius of the ith particle of the boundary particles, and N_b is the number of the boundary particle.

If a time-varying dynamic stress $\sigma(t)$ is applied to the model boundary together with a static stress value σ_s, the coupled static-dynamic loading boundary condition is given by:

$$F_i = (\sigma(t) + \sigma_s) \frac{L r_i}{\sum_{j=1}^{N_b} r_j} \tag{41}$$

During dynamic loading process, when a compressive stress wave arrives at the model boundary, a compressive or tensile stress wave will be reflected back from the fixed or free boundary. To tremendously reduce or even eliminate the influence of reflected waves on simulation results, the viscous boundary condition proposed by Lysmer and Kuhlemeyer[50] was employed to the model boundary. The basic theory of the viscous boundary is that the boundary generates a symmetric stress wave to cancel the incoming one when a wave impinges on the viscous boundary. According to the relation between velocity and stress, the symmetric stress wave can be given by:

$$\sigma = -\rho c v \tag{42}$$

where ρ and c are the medium's density and wave velocity, respectively, and v is the particle velocity.

Similarly, the width of the particle boundary must be taken into account when translating the dynamic stress into particle forces, so the force applied to every particle of viscous boundary can be expressed as:

$$F_i = -\rho c v_i \frac{L r_i}{\sum_{j=1}^{N_b} r_j} \tag{43}$$

In general, the model boundaries are mixed boundaries in which the viscous boundary coexists with the static or dynamic loading. Therefore, if the viscous boundary condition is taken into consideration, the mixed boundary condition of static stress and viscous boundary is given by:

$$F_i = (\sigma_s - \rho c v_i) \frac{L r_i}{\sum_{j=1}^{N_b} r_j} \tag{44}$$

If a dynamic load and the viscous boundary are considered simultaneously, the dynamic load magnitude must be doubled; because half of the load will be absorbed by the viscous boundary.[40] Thus the mixed boundary condition of coupled static-dynamic loading and viscous boundary is given by:

$$F_i = (2\sigma(t) + \sigma_s - \rho c v_i) \frac{L r_i}{\sum_{j=1}^{N_b} r_j} \tag{45}$$

It is worth noting that the density of the boundary particles must be set to half of its real value when the viscous boundary is considered, because only half of the particle is represented, the other half of the mass belongs to the absent particle.[40] In PFC2D, the mixed boundary conditions mentioned above can be realized using the Fish programming language. In the present study, the mixed boundary condition of coupled static-dynamic loading and viscous boundary was applied to the left boundary of the model, and the mixed boundary condition of static stress and viscous boundary was applied to the right, top and bottom boundary of the model, as illustrated in Fig. 5a.

3.3. Stress measurement and energy tracing in PFC2D

Stress is a quantity usually used in continuum mechanics and does not exist at each point in a discrete particle assembly. Stress tensors in discrete media are obtained by averaging procedures. In

PFC2D, this is realized by the stress measurement logic using a measurement circle, which was discussed in detail by Potyondy and Cundall.[49] The final expression used in PFC2D to compute the average stress tensor within a measurement circle is given by:

$$\bar{\sigma}_{ij} = -\left(\frac{1-n}{\sum_{N_p} V^{(p)}}\right) \sum_{N_p} \sum_{N_c} \left| x_i^{(c)} - x_i^{(p)} \right| n_i^{(c,p)} F_j^{(c)} \tag{46}$$

where the summations are taken over the N_p particles with centers contained within the measurement region and the N_c contacts of these particles; n is the porosity within the measurement region, $V^{(p)}$ is the volume of particle (p); $x_i^{(p)}$ and $x_i^{(c)}$ are the locations of a particle center and its contact, respectively, $n_i^{(c,p)}$ is the unit normal vector directed from a particle center to its contact location, and $F_j^{(c)}$ is the force acting at contact (c) arising from both particle contact and parallel bonds.

In PFC2D, the energy in the entire particle assembly can be tracked using the history energy command, and can also be accessed by the Fish variables that begin with e_. Nevertheless, PFC2D does not provide the source code to trace the energy within a specific region. If we want to trace the energy evolution in a specified domain, the energy measurement circle, the same as the stress measurement circle, must be applied. In the present study, we are interested in the kinetic energy and strain energy evolution around the tunnel during dynamic loading. The total kinetic energy of all particles with centers contained within the measurement circle domain can be expressed as:

$$E_k = \frac{1}{2} \sum_{N_p} \sum_{i=1}^{3} M_{(i)} v_{(i)}^2 \tag{47}$$

where N_p is the number of particles with centers contained within the measurement region, $M_{(i)}$ and $v_{(i)}$ are the generalized mass and velocity of the particles, respectively, which can be given by:

$$M_{(i)} v_{(i)} = \begin{cases} m\dot{x}_{(i)}, & for\ i = 1,2 \\ I\omega_{(3)}, & for\ i = 3 \end{cases} \tag{48}$$

where m and I are the mass and the moment of inertia of the particles, respectively, $\dot{x}_{(i)}$ and $\omega_{(i)}$ are the translational and rotational velocity of the particles.

In PFC2D, the strain energy of the material is stored in the contact and parallel-bond model. The total strain energy stored in all contacts with centers contained within the measurement circle domain can be expressed as:

$$E_c = \frac{1}{2}\sum_{N_c}\left(\left|F_i^n\right|^2 / k^n + \left|F_i^s\right|^2 / k^s\right) \tag{49}$$

where N_c is the number of contacts with centers contained within the measurement circle region; $\left|F_i^n\right|$ and $\left|F_i^s\right|$ are the magnitudes of the normal and shear components of the contact force; and k_n and k_s are the normal and shear contact stiffness.

And the total strain energy stored in all parallel bonds with centers contained within the measurement circle domain can be expressed as:

$$E_{pb} = \frac{1}{2}\sum_{N_{pb}}\left[\left|\overline{F}_i^n\right|^2 / (A\overline{k}^n) + \left|\overline{F}_i^s\right|^2 / (A\overline{k}^s) + \left|\overline{M}_3\right|^2 / (I\overline{k}^n)\right] \tag{50}$$

where N_{pb} is the number of parallel bonds with centers contained within the measurement circle region; $\left|\overline{F}_i^n\right|$ and $\left|\overline{F}_i^s\right|$ are the magnitudes of the normal and shear components of the parallel bond force, and $\left|\overline{M}_3\right|$ is the magnitude of the moment of the parallel bond; $\overline{k}^n$ and $\overline{k}^s$ are the normal and shear stiffness of the parallel bond; A and I are the area and the moment of inertia of the parallel bond, respectively.

4. Numerical simulations and results

4.1 Dynamic responses of underground tunnel induced by blasting load

In this section, a series of waveforms of blasting load with different rising time (i.e., t_r = 1 ms, 2 ms, 3 ms, 4 ms and 5 ms) and a constant t_s/t_r ratio of 5 were applied to investigate the dynamic responses of the tunnel subjected to coupled static-dynamic loading, the corresponding durations of blasting load are 5 ms, 10 ms, 15 ms, 20 ms and 25 ms. The peak value of blasting load is 15 MPa, and the vertical and horizontal in situ stress is 10 MPa. The numerical simulation results are shown in Fig. 6.

Figure 6a-c presents the tangential stress evolutional curves in different monitoring points at tunnel boundary during dynamic loading, and the positive value indicates the compressive stress. Time begins when dynamic loading was applied to the model boundary. Before dynamic stress wave arrives at tunnel boundary, stress at tunnel boundary remains constant. At t = 1.33 ms, dynamic stress wave arrives at the left sidewall of the tunnel, tangential stress at θ = π increases immediately, and then the incident compressive stress wave leads to a reduction of tangential stress at the left sidewall of the tunnel as shown in Fig. 6c. The greater the rising time of blasting load is, the larger the extent of reduction is, but when t_r

exceeds 4 ms, the extent of reduction hardly increases. Because of the existence of compressive stress induced by static stress, the reduction of tangential stress does not give rise to tensile stress at left sidewall. After the dynamic stress wave passes through, tangential stress at the left sidewall returns to initial value. When t = 1.67 ms, dynamic stress wave arrives at the roof and floor of the tunnel, tangential stress at $\theta = \pi/2$ increases rapidly as shown in Fig. 6b, and a larger rising time of blasting load brings about a higher peak value of tangential stress. When t = 2 ms, dynamic stress wave arrives at the right sidewall of the tunnel. As shown in Fig. 6a, the tangential stress evolutional curves at $\theta = 0$ are approximately the same as the curves at $\theta = \pi$. It can be found from the comparisons between Fig. 6a-c and Fig. 2 that the numerical results are generally consistent with the theoretical results, i.e. under blasting stress wave incidence, the compressive stress at $\theta = \pi/2$ is much larger than that at $\theta = 0$ and π. However, there are also some differences between theoretical and numerical results, because the theoretical solutions are based on elastodynamics, in which the rock mass is considered as homogeneous, isotropic and perfectly elastic medium, while the numerical model composes of a large number of discrete particles. Besides, the average stress in a measurement circle cannot completely represent the stress on tunnel surface.

Figure 6d-f presents the strain energy evolutional curves in different monitoring points at tunnel boundary during dynamic loading. Comparing Fig. 6a-c with Fig. 6d-f, it can be found that the strain energy evolutional curves are similar to the tangential stress evolutional curves at the same monitoring location. It denotes that the accumulation of strain energy around tunnel boundary is the result of the stress redistribution during dynamic loading. The maximum values of strain energy at $\theta = 0$ and π are 5.85 kJ and 6.65 kJ respectively, while it is 24.35 kJ at $\theta = \pi/2$. The maximum value of strain energy at $\theta = \pi/2$ is considerably larger than that at $\theta = 0$ and π, and the greater the t_r is, the larger the value of the maximum strain energy is. It indicates that a dynamic stress wave with high rising time induces a large amount of strain energy accumulating at the roof and floor of the tunnel.

Figure 6g-i presents the kinetic energy evolutional curves in different monitoring points at tunnel boundary during dynamic loading. When dynamic stress wave arrives at the left sidewall of the tunnel, the kinetic energy at $\theta = \pi$ increases rapidly to a peak value as shown in Fig. 6i, the peak value of kinetic energy decreases with the increase of t_r, and the maximum kinetic energy is 5.62 kJ when t_r = 1 ms. It can be observed from Fig. 6g and h that the peak value of kinetic energy at $\theta = 0$ and $\pi/2$ increases with the increase of t_r, and the maximum values of kinetic energy at $\theta = 0$ and $\pi/2$ are 2.66 kJ and 2.99 kJ when t_r

= 5 ms, which are smaller than that at $\theta = \pi$.

4.2 Influence of lateral pressure coefficient

In this section, the dynamic responses of an underground tunnel at a burial depth of 1000 m were examined. The vertical in situ stress is 14.74 MPa, four lateral pressure coefficients of k = 0.5, 1.0, 1.5, and 2.0 were specified to investigate the influence of lateral pressure coefficient on the dynamic responses. The rising time and total time of the blasting stress wave are 2 ms and 10 ms respectively, and the peak value of the blasting stress wave is 25 MPa. According to the analysis presented in section 4.1, the tangential stress and the strain energy have nearly the same evolution law at the same position, so only the strain energy and kinetic energy are discussed in this section. The numerical simulation results are depicted in Fig. 7.

The strain energy evolutions at different monitoring points for various lateral pressure coefficients are presented in Fig. 7a-c. Before a dynamic stress wave arrives at the tunnel boundary, the strain energy accumulated under in situ stress is related to the lateral pressure coefficient. The tangential stress derived from the Kirsch's formula[51] under in situ stress and the associated strain energy are listed in Table 3. The tangential stress and strain energy at $\theta = 0$ and π under in situ stress decrease with the increase of the lateral pressure coefficient, while those at $\theta = \pi/2$ are the opposite. It is found that the strain energy is positively related to the tangential stress accumulation. When the lateral pressure coefficient is less than 1.0, the tangential stress is mainly concentrated and thus substantial strain energy is accumulated at two sidewalls of the tunnel ($\theta = 0$ and π). But when the lateral pressure coefficient is larger than 1.0, the strain energy is mainly stored in the roof and floor. During dynamic loading process, the strain energy at $\theta = 0$ has the same evolution law as that at $\theta = \pi$ as shown in Fig. 7a and c. When the dynamic stress wave arrives at the roof and floor of the tunnel, the strain energy at $\theta = \pi/2$ goes to a peak value in a short time and then drop rapidly as shown in Fig. 7b. The greater the lateral pressure coefficient is, the higher the peak value of the strain energy is. After the dynamic stress wave passes through, the strain energy returns to the initial value for the cases of k = 0.5 and 1.0 but reduces for the cases of k = 1.5 and 2.0. It indicates that the strain energy stored in rock mass has a critical value. When the strain energy stored in rock mass exceeds its critical value, the rapid release of the strain energy occurs, accompanying with the occurrence of severe rockburst.

As presents in Fig. 7f, the lateral pressure coefficient has little influence on kinetic energy evolution at $\theta = \pi$, but it has a significant influence on kinetic energy evolution at $\theta = \pi/2$ as shown in Fig. 7e. The peak value of kinetic energy at $\theta = \pi/2$ increases with the increase of lateral pressure coefficient. After the dynamic stress wave passes through, the kinetic energy returns to zero for the case of $k = 0.5$, indicating that dynamic failure does not occur in this case; for other cases, the kinetic energy remains a constant value, indicating that the dynamic failures occur at the roof in these cases. As shown in Fig. 7d, for the cases of $k = 1.5$ and 2.0, the peak value of the kinetic energy at $\theta = 0$ are smaller than that when $k = 0.5$ and 1.0, and obvious oscillation occurs in these cases. It indicates that severe dynamic failures occur for the cases of $k = 1.5$ and 2.0, and a portion of incident energy are dissipated during dynamic failure.

The micro-crack distributions in the surrounding rock for different lateral pressure coefficients are presented in Fig. 8, the micro tensile cracks and shear cracks are respectively colored in black and red in the figure. It can be seen from the figure, a majority of micro cracks distribute at the roof and floor of the tunnel. The micro crack numbers increase with the increase of the lateral pressure coefficient. For the case of $k = 0.5$, only 5 micro cracks emerge around the tunnel. The micro cracks increase to 3061 when $k = 2.0$, and the damaged zone extends to the right side in this case.

In this study, the strain energy reduction is the difference between the initial value and final value of the strain energy evolutional curve, which denotes the release of strain energy during dynamic loading. In addition, the residual kinetic energy is defined as the final value of the kinetic energy evolutional curve, which denotes the energy carried by the ejected rock fragments during dynamic failure process of the tunnel. Therefore, the residual kinetic energy can be served as an index of the intensity of rockburst. The larger the residual kinetic energy is, the more violent the rockburst is. In order to further investigate the strain energy release law, the strain energy reduction and the residual kinetic energy at $\theta = \pi/2$ are summarized in Fig. 9. The strain energy reduction and residual kinetic energy at $\theta = \pi/2$ increase with the increase of the lateral pressure coefficient. Because no failure occurs for the case of $k = 0.5$, the strain energy reduction and residual kinetic energy are zero. When $k = 2.0$, the strain energy reduction and residual kinetic energy reach to 28.63 kJ and 78.66 kJ, and the strain energy reduction accounts for 98.52% of the initial strain energy (the initial value is 29.06 kJ as presented in Fig. 7b). It denotes that the majority of the strain energy stored in the roof of the tunnel released after dynamic loading, and serious damages generated at the roof of the tunnel, which is consistent with Fig. 8. It can also be seen from Fig. 9

that the residual kinetic energy is far larger than the strain energy reduction for the same condition if dynamic failure occurs at tunnel boundary, because the residual kinetic energy derives not only from strain energy release but also from incident stress wave. In this regard, it can be inferred that the rockburst hazard triggered by dynamic loading is more violent than that induced by in situ stress unloading, in which the residual kinetic energy only comes from strain energy release.

Simulation results discussed in this section suggest that the in situ stress dominates the strain energy distribution around the tunnel, and the dynamic stress wave is an external factor to trigger dynamic failures in the periphery of the tunnel. The roof and floor of the tunnel are more vulnerable to dynamic failures in this condition. With small lateral pressure coefficient, dynamic failures rarely emerge at the roof and floor of the tunnel due to a little amount of strain energy is accumulated under static stress. With the increase of lateral pressure coefficient, more strain energy is stored in the roof and floor and it may reach the critical level. In this case, dynamic loading can trigger violent dynamic failures associated with the release of substantial strain energy. Therefore, it is very significant to consider the influence of lateral pressure coefficient in order to investigate the dynamic behaviors induced by blasting load.

4.3 Influence of the burial depth of tunnel and the amplitude of the blasting load

As the excavated depth of the underground tunnel goes deeper, the tunnel will be positioned at a higher in situ stress level, leading to more strain energy to accumulate at the periphery of the tunnel. Therefore, in situ stress levels have a significant influence on the stability of the underground tunnel. In addition, the amplitude of the blasting load is also an important factor to trigger dynamic failure of the underground tunnel. In this section, four burial depths (i.e. depth = 0 m, 500 m, 1000 m, 1500 m) and three amplitudes of the blasting load (i.e. P_{bm} = 20 MPa, 30 MPa, 40 MPa) were considered to investigate the effects of in situ stress levels and amplitudes of the blasting load on the stability of the underground tunnel. According to section 4.2, it is easier to induce failure by dynamic loading under the condition of high lateral pressure coefficient, so the axial direction of the tunnel was assumed to extend along the maximum horizontal principle. In this case, the vertical and horizontal in situ stress for different burial depths can be determined from Eqs. (35) - (37), i.e. $\sigma_v = \sigma_h = 0$ MPa at 0 m; $\sigma_v = 7.74$ MPa, $\sigma_h = 10.33$ MPa at 500 m; $\sigma_v = 14.74$ MPa, $\sigma_h = 18.83$ MPa at 1000 m; $\sigma_v = 21.74$ MPa, $\sigma_h = 27.33$ MPa at 1500 m. The rising time and total time of the blasting load are 2 ms and 10 ms, respectively. According to the analysis results mentioned above, dynamic failure is more likely to occur at the roof and floor of the tunnel, so only the strain energy evolutional curves at $\theta = \pi/2$ of the tunnel are discussed in this section.

Figure 10 presents the strain energy evolutional curves at $\theta = \pi/2$ of the tunnel at different depths. The higher in situ stress results in more strain energy accumulating at the roof of the tunnel. Under dynamic loading, the strain energy at $\theta = \pi/2$ increases rapidly, and the peak value of the strain energy increases with the increase of the amplitude for a specified burial depth. During dynamic loading process, if the strain energy stored in the measuring domain reaches the critical level, the strain energy evolutional curve will oscillate and drop in a short time, and the shorter dropping time denotes the rapider release of the strain energy.

Figure 11 presents the strain energy reduction and residual kinetic energy at $\theta = \pi/2$ of the tunnel. The strain energy reduction and residual kinetic energy increase with the increase of the burial depth. For a specified depth, the increase of the amplitude of the blasting load results in more strain energy reduction and residual kinetic energy. But the strain energy reduction is zero when the depth of the tunnel is 0 m, as none of strain energy is stored in the surrounding rock before dynamic loading. In this case, the residual kinetic energy only comes from the blasting load. When the burial depth of the tunnel exceeds 1000 m, a smaller amplitude of blasting load (P_{bm} = 30 MPa) is sufficient to trigger complete failures at the roof of the tunnel. It can also be found from Fig. 11 that the residual kinetic energy is far larger than the strain energy reduction under the same condition.

Figure 12 illustrates the crack distributions in the surrounding rock at different depths and under blasting load with different amplitudes, the micro tensile cracks and shear cracks are respectively colored in black and red. It can be seen from Fig. 12 that, if the dynamic loading is only considered, the tensile cracks appear in two sidewalls of the tunnel when P_{bm} = 40 MPa, as well as a few micro cracks distribute at the roof and floor. When the burial depth of the tunnel goes to 500 m, the tensile crack only emerges in the left sidewall and more micro cracks distribute at the roof and floor. At the depth of 1000 m and 1500 m, the tensile crack disappears, and the evident damaged zones occur at the roof and floor, which extend to the right sidewall of the tunnel for the cases of P_{bm} = 40 MPa. For a specified burial depth, the extent of damaged zone increases with the increase of the amplitude of the blasting load, because the blasting load with larger amplitude contains more incident energy and can trigger more violent dynamic failures around the tunnel. For an underground tunnel subjected to the blasting load with specified amplitude, the extent of the damaged zone increases with the increase of the burial depth of the tunnel. In particular, for the tunnel at the depth of 1500 m, the dynamic loading with lower amplitude (P_{bm} = 20 MPa) is sufficient to trigger dramatic dynamic failures at the roof and floor of the tunnel.

5 Discussion

In the present study, the theoretical formulations were obtained to accurately assess the dynamic stress concentration factor around a circular tunnel subjected to blasting stress wave, and the entire process of stress wave propagating through an underground tunnel was modeled using a numerical model. The numerical results showed that the in situ stress environment has a significant effect on the dynamic responses of the underground tunnel. The blasting load can induce dramatic dynamic effects around the underground tunnel and is likely to trigger severe rockbursts in tunnel surface. As stated by Li and Weng[36] that the strain energy distribution in tunnel boundary is related to the lateral pressure coefficient, and the strain energy is mainly stored in compressive stress concentration zone under static stress. Their results indicated that when the lateral pressure coefficient is less than 1.0, two sidewalls of the opening are subjected to high compressive stress, which results in high strain energy intensity near the sidewalls. But when the lateral pressure coefficient is larger than 1.0, the strain energy mainly intensifies at the roof and floor. In the present study, the conclusions from section 4.2 are consistent with their results. Besides, the numerical results shown in Figs. 9 and 11 further indicate that the strain energy release is positively related to the lateral pressure coefficient and the burial depth of the tunnel. However, when a non-circular cross section is used in an underground tunnel, the strain energy distribution is more complicated. In this case, the strain energy release is also related to the in situ stress orientation[46] and the incident direction of the blasting stress wave,[35, 36] and different conclusions can be drawn when the blasting stress wave was applied to the model boundary from different directions.

In addition, numerical simulation results of Li and Weng[36] and Zhu et al. [35] showed that the dynamic failures mainly emerge in the incident side of the opening under dynamic disturbance. The dynamic failures in the present model mainly emerged in the positions perpendicular to the incident direction of blasting stress wave (i.e. the roof and floor of the tunnel, as shown in Figs. 8 and 12), it seems that our findings are inconsistent with the their results. However, as proposed by Wang and Cai[37] that the ratio of incident wavelength to excavation span (λ/D) has a large effect on ground motion around excavations, and the stress field near excavation boundary becomes very complex as the λ/D ratio decreases. Therefore, the incident waves with different wavelengths may lead to different failure modes around underground tunnel. When a high-frequency stress wave propagates through a circular tunnel, the circular boundary appears to be a plane boundary. In this case, the incident compressive stress wave is reflected back as the tensile one, which will lead to the spalling failures in the incident side. If the incident stress wave is a low-frequency one, the stress states around the tunnel approach to the static loading conditions. In this case, the positions perpendicular to the incident direction are more prone to failures.

In the present analysis, the equivalent wavelength of a triangular wave can be calculated by $\lambda = t_s c_p$, where t_s is the duration of blasting load and c_p is the longitudinal wave velocity, which is 3000 m/s in this study. Previous studies[35, 36] on stability of underground tunnels induced by dynamic disturbance focused on a small λ/D ratio ($\lambda/D < 1$), in this case, dynamic failures mainly occurred in the incident side. In this study, the duration of blasting load used in sections 4.2 and 4.3 is 10 ms, and the corresponding λ/D ratio is 15. In this case, the dynamic failures mainly occurred in the roof and floor. However, because of the diversities of blasting parameters and tunnel dimensions, the λ/D ratio may vary in a wide range. Therefore, it is necessary to discuss the stability of underground tunnels under conditions of different λ/D ratios. The ratio of incident wavelength to excavation span may have a significant influence on the failure characteristics of the tunnel, especially complicated geological environments and tunnel cross-section shapes are considered at the same time. In our future study, we plan to take the stress wave propagation and attenuation into consideration and further investigate the influence of the incident wavelength and the tunnel cross-section shape on fracturing characteristics of the deep-buried tunnel. These will be further introduced in our following paper.

6. Conclusions

In this paper, a two-dimensional mathematical physics model was first presented to investigate the dynamic response around a circular tunnel subjected to blasting stress wave excitation. Based on the steady state solution of the wave expansion approach, transient solutions subjected to different incident waveforms were obtained. Theoretical results indicated that the DSCF at the roof and floor of the tunnel is much larger than that at two sidewalls when blasting stress wave was applied to left model boundary, but the dynamic amplification factor at two sidewalls is much larger than that at the roof and floor. A two-dimensional numerical model established by the discrete element program PFC2D was then introduced to verify the theoretical analysis, and to further explore the energy evolution law around the underground tunnel subjected to coupled static-dynamic loading. The numerical results indicated that, for an underground tunnel only subjected to in situ stress, high compressive stress concentration around the tunnel leads to the accumulation of massive strain energy at the same location. During dynamic loading process, the roof and floor of the tunnel are more vulnerable to dynamic failures. The larger the lateral pressure coefficient is, the more strain energy and kinetic energy release during dynamic failures. In addition, the residual kinetic energy is much larger than the strain energy release under the same condition. Furthermore, for an underground tunnel subjected to high in situ stress, the dynamic loading with lower amplitude is sufficient to trigger severe dynamic failures. Therefore, the effect of the dynamic blasting stress wave induced by adjacent tunnel excavations should be taken into consideration when the support and reinforcement systems of an underground tunnel are designed, especially for the tunnel subjected to high in situ stress.

Acknowledgements

The authors would like to thank the financial support from the National Natural Science Foundation of China (Grant No. 11472311 and 41630642) and the State Key Research Development Program of China (Grant No. 2016YFC0600706).

References

1. Jiang Q, Feng XT, Chen J, Huang K, Jiang YL. Estimating in-situ rock stress from spalling veins: A case study. Eng Geol. 2013;152(1):38-47.
2. Cai M, Kaiser PK. In-situ rock spalling strength near excavation boundaries. Rock Mech Rock Eng. 2014;47(2):659-675.
3. Shemyakin EI, Fisenko GL, Kurlenya MV, Oparin VN, Reva VN, Glushikhin FP, Rozenbaum MA, Tropp EA, Kuznetsov YS. Zonal disintegration of rocks around underground workings, Part 1: Data of in situ observations. Sov Min. 1986;22(3):157-168.
4. Jia P, Zhu WC. Mechanism of zonal disintegration around deep underground excavations under triaxial stress – Insight from numerical test. Tunn Undergr Space Technol. 2015;48(11):1-10.
5. Ortlepp WD, Stacey TR. Rockburst mechanisms in tunnels and shafts. Tunn Undergr Space Technol. 1994;9(1):59-65.
6. Li SJ, Feng XT, Li ZH, Chen BR, Zhang CQ, Zhou H. In situ monitoring of rockburst nucleation and evolution in the deeply buried tunnels of Jinping II hydropower station. Eng Geol. 2012;137-138(7):85-96.
7. Cai M. Influence of stress path on tunnel excavation response – Numerical tool selection and modeling strategy. Tunn Undergr Space Technol. 2008;23(6):618-628.
8. Lu WB, Yang JH, Yan P, Yan P, Chen M, Zhou CB, Luo Y, Jin L. Dynamic response of rock mass induced by the transient release of in-situ stress. Int J Rock Mech Min Sci. 2012;53(9):129-141.
9. Yang JH, Yao C, Jiang QH, Lu WB, Jiang SH. 2D numerical analysis of rock damage induced by dynamic in-situ stress redistribution and blast loading in underground blasting excavation. Tunn Undergr Space Technol. 2017;70:221-232.
10. Fan Y, Lu WB, Yan P, Chen M, Zhang YZ. Transient characters of energy changes induced by blasting excavation of deep-buried tunnels. Tunn Undergr Space Technol. 2015;49:9-17.
11. Weng L, Huang LQ, Taheri A, Li XB. Rockburst characteristics and numerical simulation based on a strain energy density index: A case study of a roadway in Linglong gold mine, China. Tunn Undergr Space Technol. 2017;69:223-232.
12. Germanovich LN, Dyskin AV. Fracture mechanisms and instability of openings in compression.

Int J Rock Mech Min Sci. 2000;37(1):263-284.

13. Martino JB, Chandler NA. Excavation-induced damage studies at the Underground Research Laboratory. Int J Rock Mech Min Sci. 2004;41(8):1413-1426.

14. Read RS. 20 years of excavation response studies at AECL's Underground Research Laboratory. Int J Rock Mech Min Sci. 2004;41(8):1251-1275.

15. Golshani A, Oda M, Okui Y, Takemura T, Munkhtogoo E. Numerical simulation of the excavation damaged zone around an opening in brittle rock. Int J Rock Mech Min Sci. 2007;44(6):835-845.

16. Zhu WC, Bruhns OT. Simulating excavation damaged zone around a circular opening under hydromechanical conditions. Int J Rock Mech Min Sci. 2008;45(5):815-830.

17. Wang HW, Jiang YD, Xue S, Shen BT, Wang C, L JG, Yang T. Assessment of excavation damaged zone around roadways under dynamic pressure induced by an active mining process. Int J Rock Mech Min Sci. 2015;77:265-277.

18. Shin JH, Moon HG, Chae SE. Effect of blast-induced vibration on existing tunnels in soft rocks. Tunn Undergr Space Technol. 2011;26(1):51-61.

19. Liang QG, Li J, Li DW, Ou E. Effect of blast-induced vibration from new railway tunnel on existing adjacent railway tunnel in xinjiang, China. Rock Mech Rock Eng. 2013;46(1):19-39.

20. Yu HT, Yuan Y, Yu GX, Liu X. Evaluation of influence of vibrations generated by blasting construction on an existing tunnel in soft soils. Tunn Undergr Space Technol. 2014;43(7):59-66.

21. Ainalis D, Kaufmann O, Tshibangu JP, Verlinden O, Kouroussis G. Modelling the source of blasting for the numerical simulation of blast-induced ground vibrations: A review. Rock Mech Rock Eng. 2017;50(1):171-193.

22. Hao H, Wu C, Seah CC. Numerical analysis of blast-induced stress waves in a rock mass with anisotropic continuum damage models part 2: Stochastic approach. Rock Mech Rock Eng. 2002;35(2):95-108.

23. Wu CQ, Lu Y, Hao H. Numerical prediction of blast-induced stress wave from large-scale underground explosion. Int J Numer Anal Met. 2004;28(1):93-109.

24. Malmgren L, Nordlund E. Behaviour of shotcrete supported rock wedges subjected to blast-induced vibrations. Int J Rock Mech Min Sci. 2006;43(4):593-615.

25. Dhakal RP, Pan TC. Response characteristics of structures subjected to blasting-induced ground motion. Int J Impact Eng. 2003;28(8):813-828.
26. Chen HL, Xia ZC, Zhou JN, Fan HL, Jin FN. Dynamic responses of underground arch structures subjected to conventional blast loads: Curvature effects. Arch Civ Mech Eng. 2013;13(3):322-333.
27. Mitelman A, Elmo D. Analysis of tunnel support design to withstand spalling induced by blasting. Tunn Undergr Space Technol. 2016;51:354-361.
28. Jing L, Hudson JA. Numerical methods in rock mechanics. Int J Rock Mech Min Sci. 2002;39(4):409-427.
29. Jing L. A review of techniques, advances and outstanding issues in numerical modelling for rock mechanics and rock engineering. Int J Rock Mech Min Sci. 2003;40(3):283-353.
30. Stamos AA, Beskos DE. Dynamic analysis of large 3-D underground structures by the BEM. Earthq Eng Struct D. 1995;24(6):917-934.
31. Wang ZL, Li YC, Shen RF. Numerical simulation of tensile damage and blast crater in brittle rock due to underground explosion. Int J Rock Mech Min Sci. 2007;44(5):730-738.
32. Ning YJ, Yang J, An XM, Ma GW. Modelling rock fracturing and blast-induced rock mass failure via advanced discretisation within the discontinuous deformation analysis framework. Comput Geotech. 2011;38(1):40-49.
33. Ning YJ, Yang J, Ma GW, Chen PW. Modelling rock blasting considering explosion gas penetration using discontinuous deformation analysis. Rock Mech Rock Eng. 2011;44(4):483-490.
34. Wang TT, Yang CH, Yan XZ, Li YP, Liu W, Liang C, Li J. Dynamic response of underground gas storage salt cavern under seismic loads. Tunn Undergr Space Technol. 2014;43(7):241-252.
35. Zhu WC, Li ZH, Zhu L, Tang CA. Numerical simulation on rockburst of underground opening triggered by dynamic disturbance. Tunn Undergr Space Technol. 2010;25(5):587-599.
36. Li XB, Weng L. Numerical investigation on fracturing behaviors of deep-buried opening under dynamic disturbance. Tunn Undergr Space Technol. 2016;54:61-72.
37. Wang X, Cai M. Influence of wavelength-to-excavation span ratio on ground motion around deep underground excavations. Tunn Undergr Space Technol. 2015;49:438-453.

38. Wang ZL, Konietzky H, Shen RF. Coupled finite element and discrete element method for underground blast in faulted rock masses. Soil Dyn Earthq Eng. 2009;29(6):939-945.
39. An HM, Liu HY, Han H, Zheng X, Wang XG. Hybrid finite-discrete element modelling of dynamic fracture and resultant fragment casting and muck-piling by rock blast. Comput Geotech. 2017;81:322-345.
40. Resende R, Lamas LN, Lemos JV, Calçada R. Micromechanical modelling of stress waves in rock and rock fractures. Rock Mech Rock Eng. 2010;43(6):741-761.
41. Huang XL, Qi SW, Williams A, Zou Y, Zheng BW. Numerical simulation of stress wave propagating through filled joints by particle model. Int J Solids Struct. 2015;69-70:23-33.
42. Li XB, Cao WZ, Zhou ZL, Zou Y. Influence of stress path on excavation unloading response. Tunn Undergr Space Technol. 2014;42(42):237-246.
43. Cao WZ, Li XB, Tao M, Zhou ZL. Vibrations induced by high initial stress release during underground excavations. Tunn Undergr Space Technol. 2016;53:78-95.
44. Li XB, Cao WZ, Tao M, Zhou ZL, Chen ZH. Influence of unloading disturbance on adjacent tunnels. Int J Rock Mech Min Sci. 2016;84:10-24.
45. Pao YH, Mow CC. Diffraction of elastic waves and dynamic stress concentrations. Crane Russak; 1973.
46. Weng L, Li XB, Tao M. Influence of geostress orientation on fracture response of deep underground cavity subjected to dynamic loading. Shock Vib. 2015;2015(1):1-9.
47. Stovel RT. Approximate techniques for determining transient solutions. Cornell University; 1967.
48. Tao M, Ma A, Cao WZ, Li XB, Gong FQ. Dynamic response of pre-stressed rock with a circular cavity subject to transient loading. Int J Rock Mech Min Sci. 2017;99:1-8.
49. Potyondy DO, Cundall PA. A bonded-particle model for rock. Int J Rock Mech Min Sci. 2004;41(8):1329-1364.
50. Lysmer J, Kuhlemeyer RL. Finite dynamic model for infinite media. J Eng Mech Div ASCE. 1969;95(4):859-878.
51. Brady BHG, Brown ET. Rock mechanics for underground mining. Berlin: Springer; 2004.

Figures and Tables

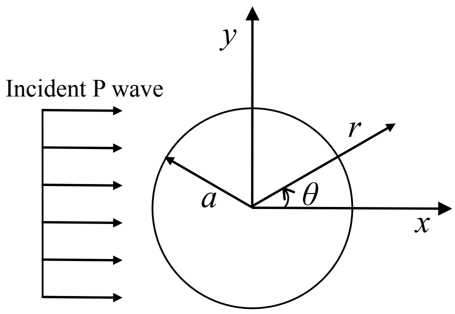

Fig. 1. Simplified model of interactions between incident P wave and underground tunnel.

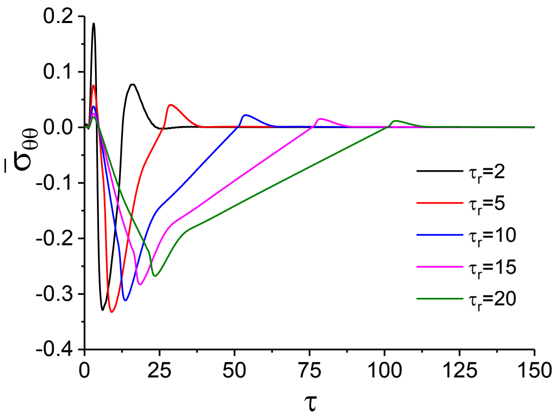

(a) $\theta = 0$, $t_s/t_r = 5$

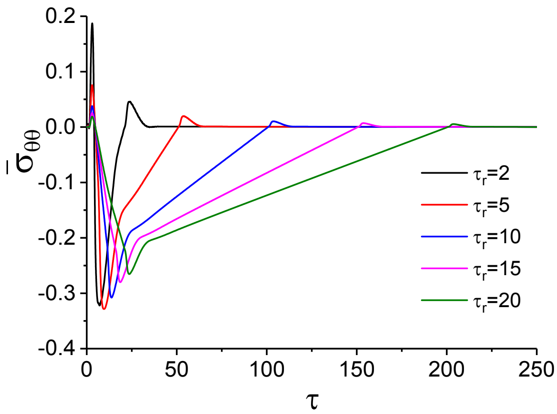

(b) $\theta = 0$, $t_s/t_r = 10$

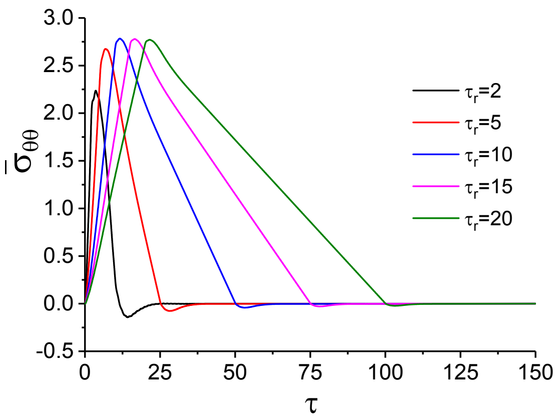

(c) $\theta = \pi/2$, $t_s/t_r = 5$

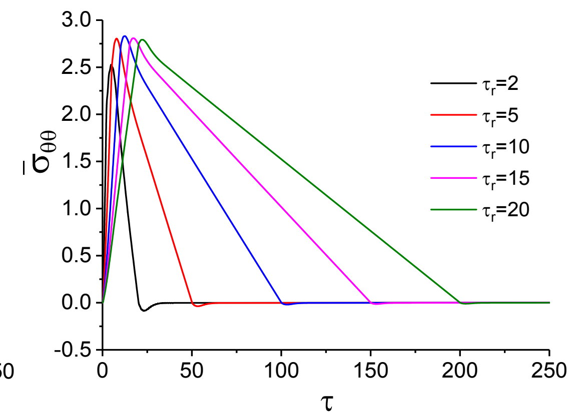

(d) $\theta = \pi/2$, $t_s/t_r = 10$

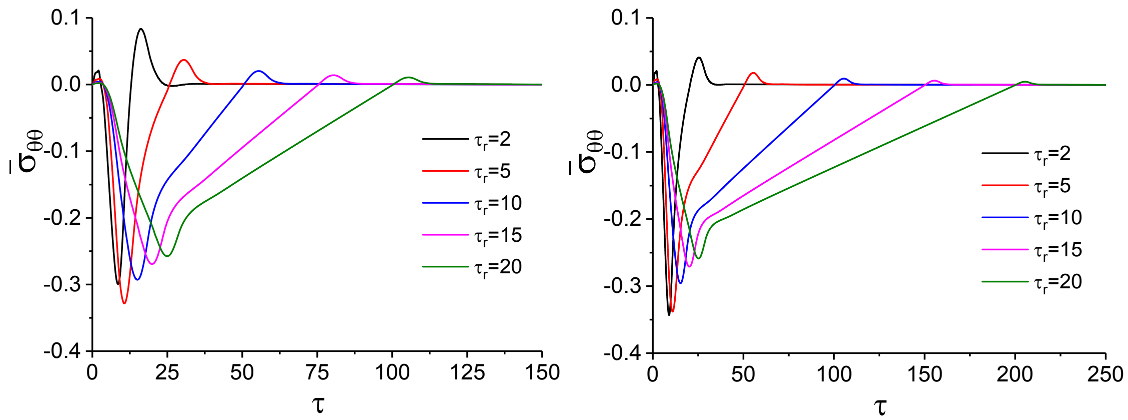

(e) $\theta = \pi$, $t_s/t_r = 5$ (f) $\theta = \pi$, $t_s/t_r = 10$

Fig. 2. Numerical results of the DSCF at tunnel boundary.

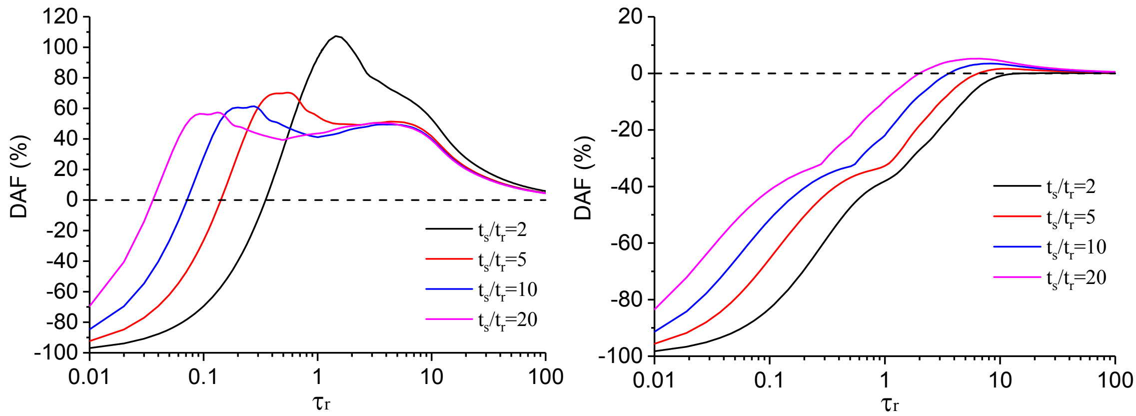

(a) $\theta = 0$ (b) $\theta = \pi/2$

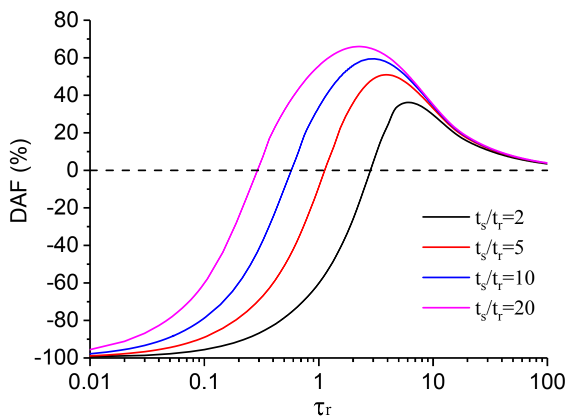

(c) $\theta = \pi$

Fig. 3. Dynamic amplification factors at tunnel boundary.

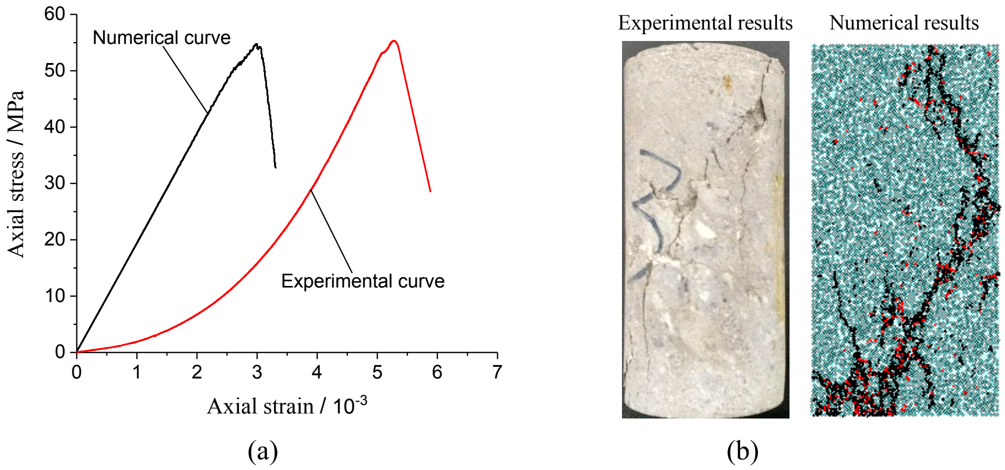

Fig. 4. Comparison between experimental and numerical results of the rock specimen under uniaxial compression: (a) stress-stain curve and (b) final failure mode.

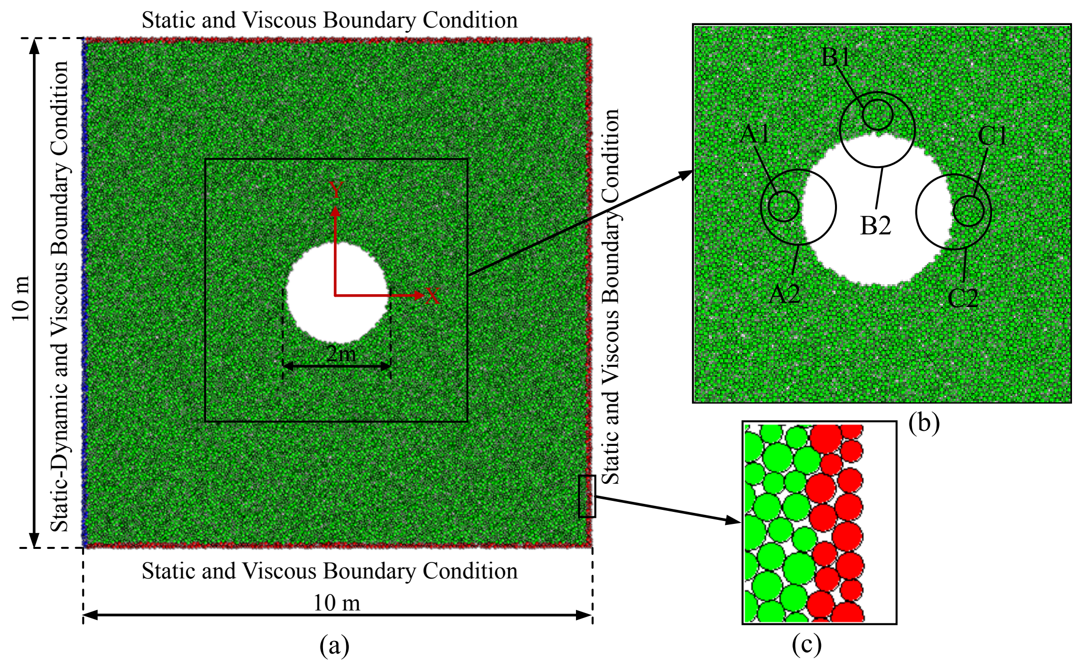

Fig. 5. Schematic diagram of the PFC2D numerical model: (a) Boundary conditions; (b) Layout of measurement circles (A1, B1 and C1 are stress measurement circles; A2, B2 and C2 are energy measurement circles); (c) Model boundary particles.

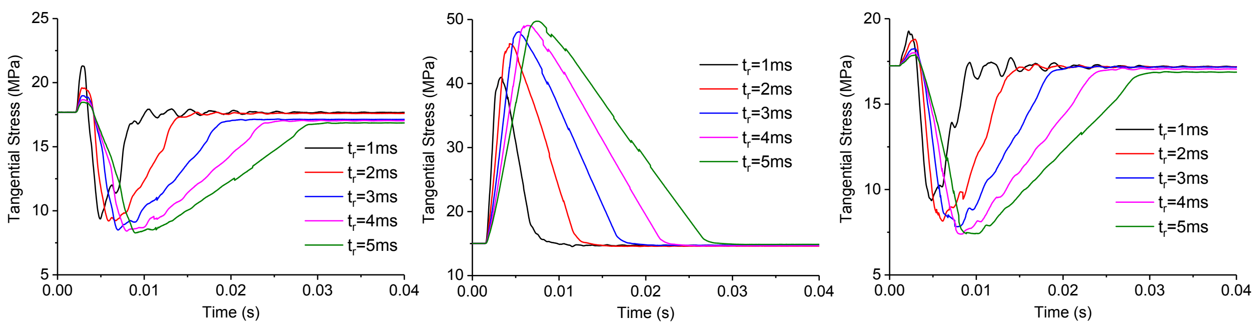

(a) $\theta = 0$ (b) $\theta = \pi/2$ (c) $\theta = \pi$

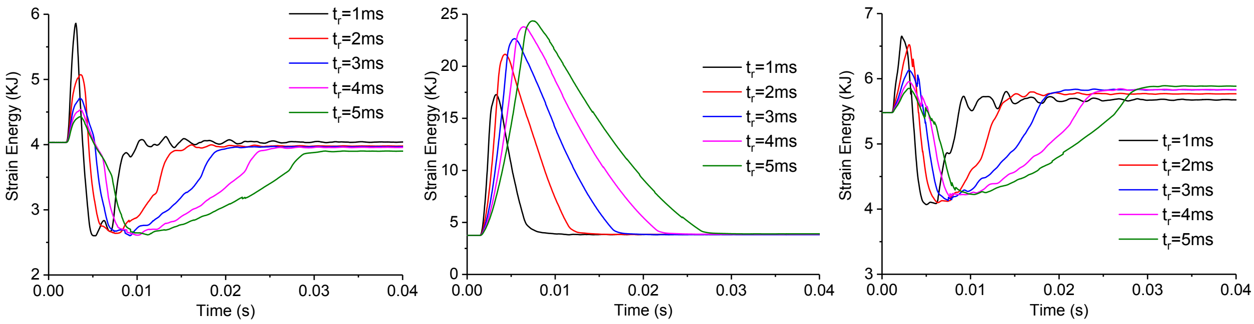

(d) $\theta = 0$ (e) $\theta = \pi/2$ (f) $\theta = \pi$

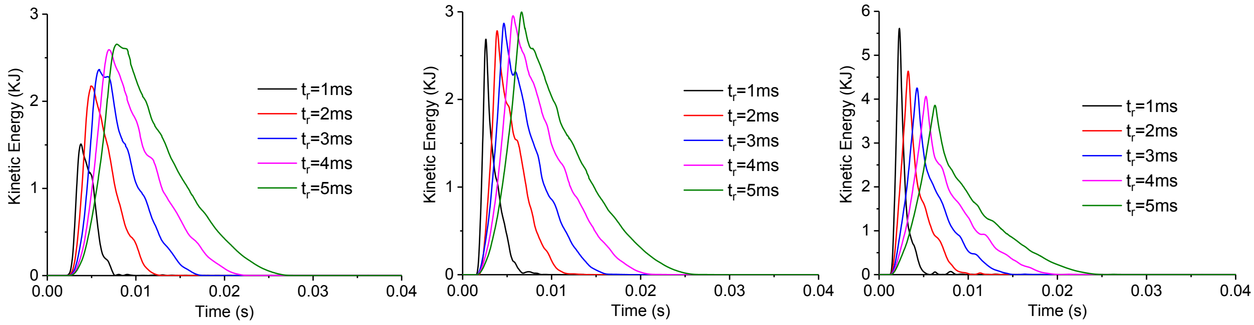

(g) $\theta = 0$ (h) $\theta = \pi/2$ (i) $\theta = \pi$

Fig. 6. Stress and energy evolutional curves at different monitoring points under various waveforms of blasting load ((a)、(b)、(c): tangential stress evolution, (d)、(e)、(f): strain energy evolution, (g)、(h)、(i): kinetic energy evolution).

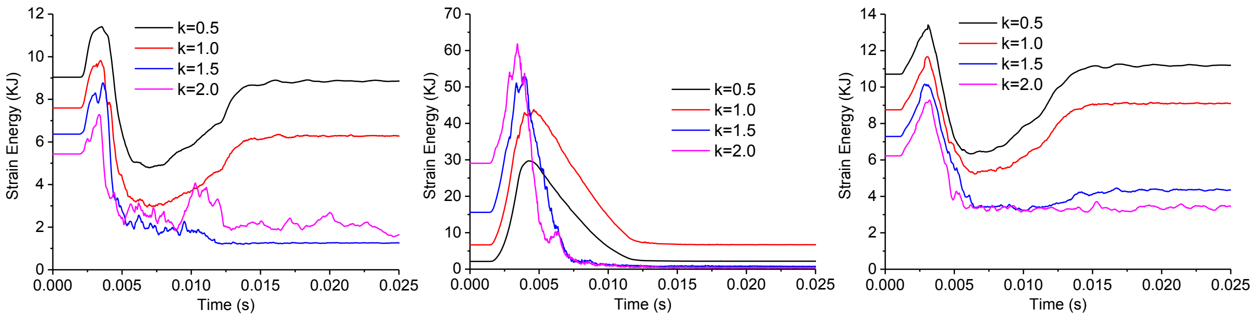

(a) $\theta = 0$ (b) $\theta = \pi/2$ (c) $\theta = \pi$

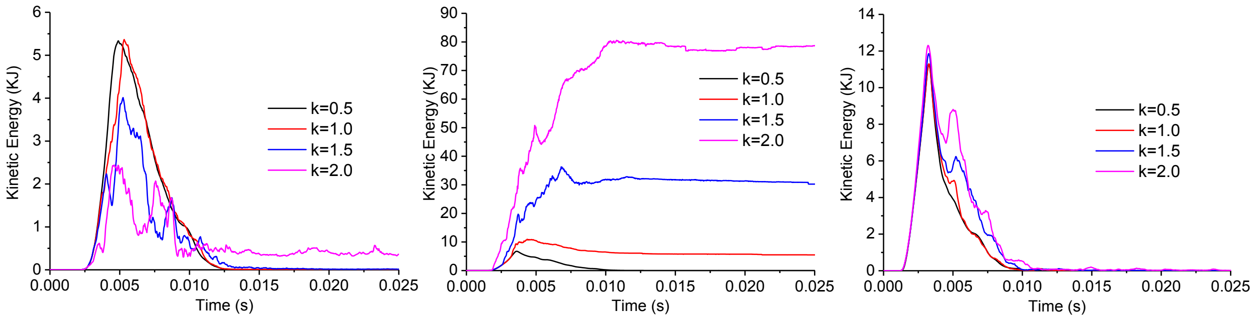

(d) $\theta = 0$ (e) $\theta = \pi/2$ (f) $\theta = \pi$

Fig. 7. Energy evolutional curves at different monitoring points for various lateral pressure coefficients ((a)、(b)、(c): strain energy evolution, (d)、(e)、(f): kinetic energy evolution).

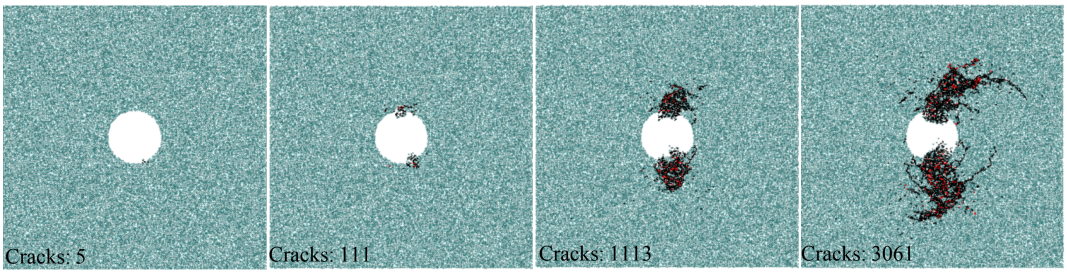

(a) $k = 0.5$ (b) $k = 1.0$ (c) $k= 1.5$ (d) $k = 2.0$

Fig. 8. Crack distributions in the surrounding rock for various lateral pressure coefficients (black and red denote tensile and shear cracks).

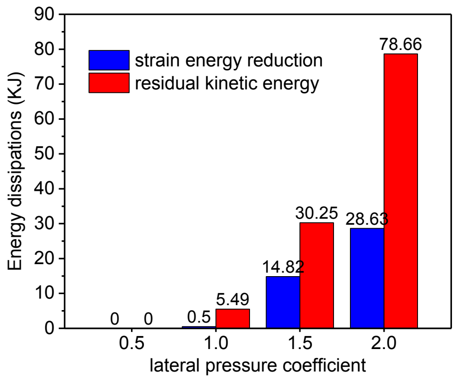

Fig. 9. Energy dissipations at $\theta = \pi/2$ of the tunnel for various lateral pressure coefficients.

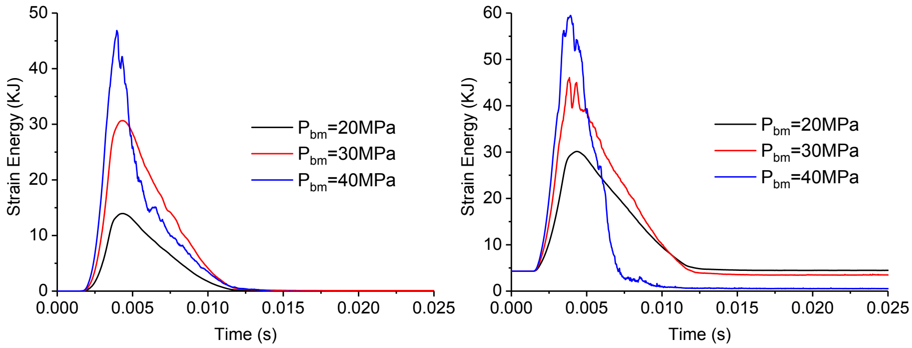

(a) Depth = 0 m (b) Depth = 500 m

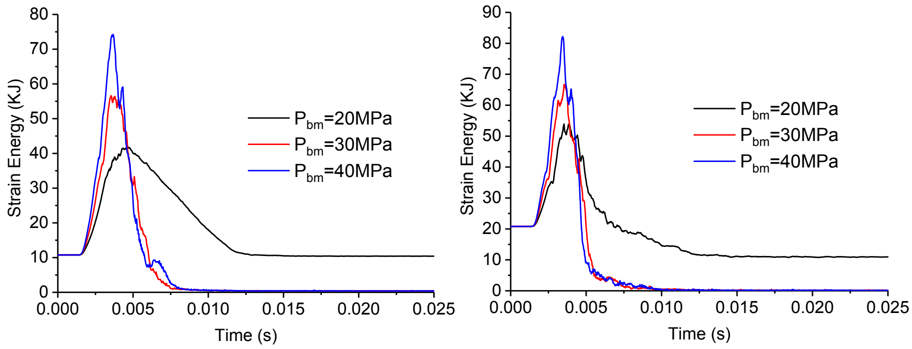

(c) Depth = 1000 m (d) Depth = 1500 m

Fig. 10. Strain energy evolutional curves at $\theta = \pi/2$ of the tunnel at different depths and under blasting load with different amplitudes.

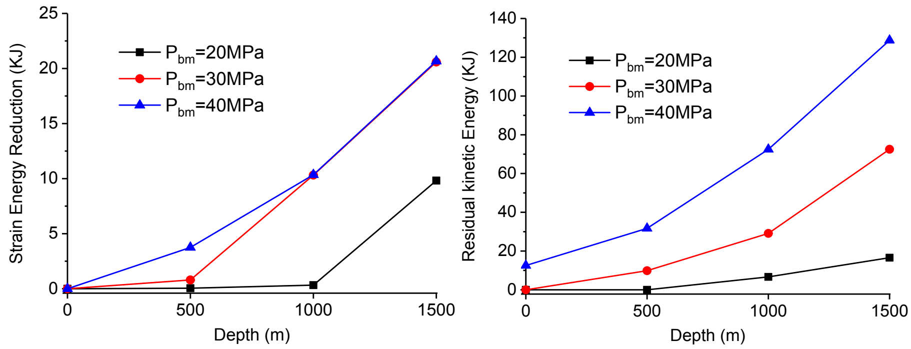

(a) (b)

Fig. 11. Energy dissipations at $\theta = \pi/2$ of the tunnel at different depths and under blasting load with different amplitudes: (a) strain energy reduction and (b) residual kinetic energy.

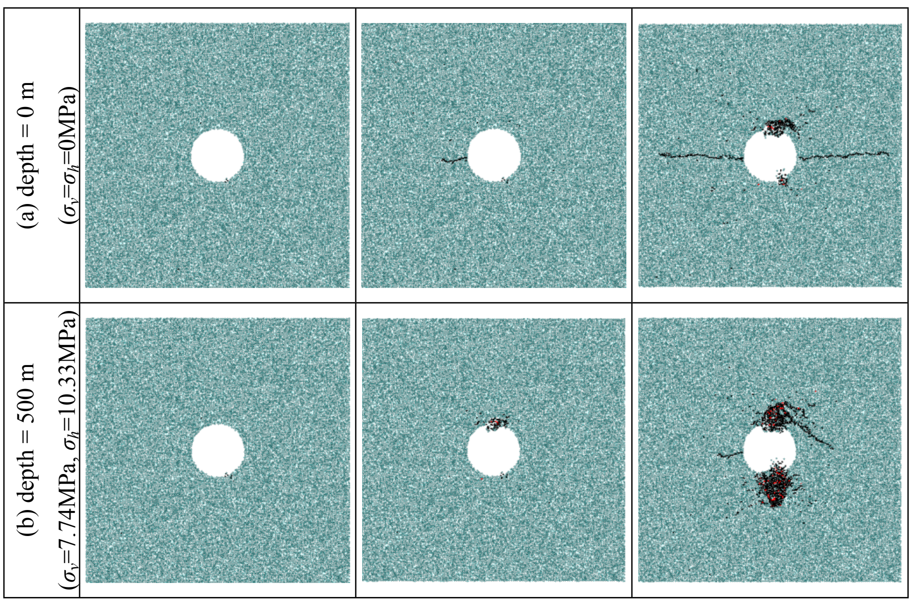

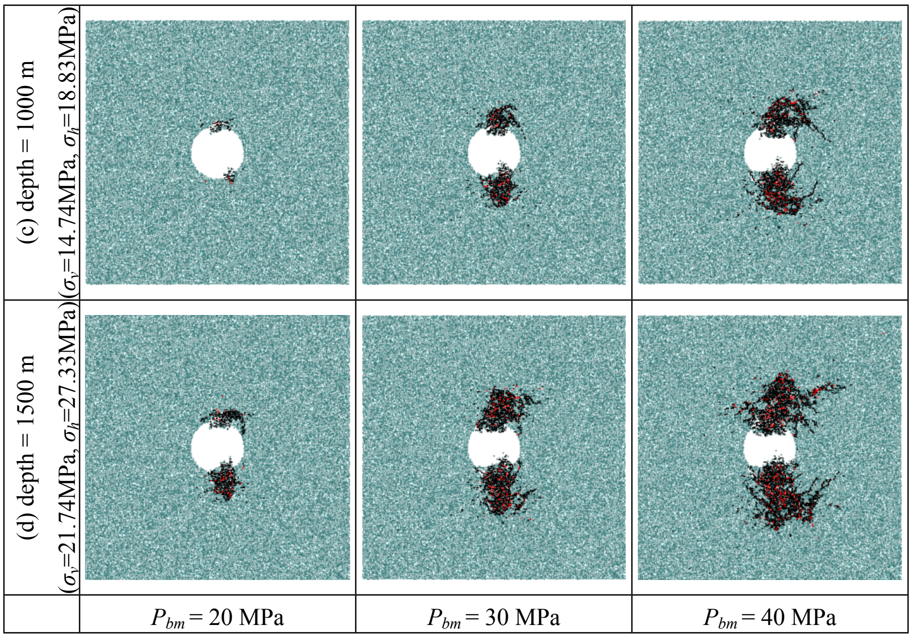

Fig. 12. Crack distributions in the surrounding rock at different depths and under blasting load with different amplitudes.

Table 1

Comparison between the experimental and numerical mechanical parameters for rock specimen.

Mechanical parameters	Physical model	Numerical results	Error (±%)
Density, ρ (kg/m^3)	2750	2989	-
Uniaxial compressive Strength, UCS (MPa)	55.32	54.77	0.99
Young's modulus, E (GPa)	18.73	18.84	0.59
Poisson's ratio, v	0.206	0.204	0.97

Table 2

The microscopic parameters of the PFC model.

Particle basic parameters	value
Particle density, ρ (kg/m^3)	2989
Particle minimum radius, r_{min} (m)	2×10^{-4}
Particle radius ratio, r_{max}/r_{min}	2
Particle contact module, E_c (GPa)	15.87
Particle Stiffness ratio, k_n/k_s	2.0

Particle friction coefficient, μ	0.5
Parallel-bond parameters	
Parallel-bond radius multiplier, $\bar{\lambda}$	1
Parallel-bond modulus, $\bar{E}_c$ (GPa)	15.87
Parallel-bond stiffness ratio, $\bar{k}_n / \bar{k}_s$	2.0
Mean normal strength, $\bar{\sigma}$ (MPa)	45.27
Std.dev. of normal strength, $\bar{\sigma}_s$ (MPa)	9.05
Mean shear strength, $\bar{\tau}$ (MPa)	45.27
Std.dev. of shear strength, $\bar{\tau}_s$ (MPa)	9.05

Table 3
Tangential stress and strain energy induced by in situ stress for various lateral pressure coefficients.

k	$\theta = 0$		$\theta = \pi/2$		$\theta = \pi$	
	Tangential stress (MPa)	Strain energy (kJ)	Tangential stress (MPa)	Strain energy (kJ)	Tangential stress (MPa)	Strain energy (kJ)
0.5	36.85	9.04	7.37	2.13	36.85	10.71
1.0	29.48	7.59	29.48	6.66	29.48	8.75
1.5	22.11	6.37	51.59	15.58	22.11	7.29
2.0	14.74	5.43	73.70	29.05	14.74	6.22